

学位論文(要約)

Carrier Transport in Perovskite-type Oxynitride and
Its Control by Epitaxial Growth Technique

(ペロブスカイト型酸窒化物におけるキャリア輸送と
エピタキシャル成長技術によるその制御)

平成 29 年 12 月博士(理学)申請

東京大学大学院理学系研究科

化学専攻

佐野 真仁

Carrier Transport in Perovskite-type Oxynitride and
Its Control by Epitaxial Growth Technique

by

Masahito Sano

Development of Chemistry
Graduate School of Science
The University of Tokyo

December. 2017

Abstract

Perovskite-type oxide, which is one group of metal oxides, has been intensively studied in terms of development of new functionality by substitution of cations. Recently, substitution of non-metal elements for oxygen attracts attention as a new way to realize novel functionalities. Oxynitride is one group of mixed anion compounds, and it has been of interest for its optical properties toward high efficiency photocatalysts and non-toxic pigments with visible light absorption. On the other hand, studies on their intrinsic transport properties have been limited by extrinsic factors originating from the shape of samples, because oxynitride has been conventionally synthesized only in polycrystalline powder form. To overcome this problem, I focused on epitaxial growth of oxynitride single crystalline thin films.

For investigation of intrinsic transport properties, I focused on $\text{LaVO}_{3-x}\text{N}_x$ (LVON). Its mother material LaVO_3 is known to show insulator-to-metal transition (IMT) by hole-doping through substitution of Ca^{2+} or Sr^{2+} for La^{3+} . In contrast, LVON bulk polycrystal was reported not to show IMT even if a large number of holes were doped, suggesting specific transport properties different from cation-substituted compounds. However, influence of extrinsic factors such as grain boundary could not be excluded.

In this study, I synthesized LVON single crystalline thin films ($0 \leq x \leq 0.71$) on lattice matched single crystalline substrate using nitrogen-plasma-assisted pulsed laser deposition (NPA-PLD) method. The obtained LVON thin films exhibited resistivity (ρ) of 2 or 3 orders of magnitude lower than those of bulk polycrystals, indicating suppressed contribution of grain boundaries to ρ . On the other hand, the LVON thin films did not show IMT even for much higher doping level than cation-substituted metallic LaVO_3 . From the results, I concluded that carrier localization is an intrinsic feature of LVON. To investigate the mechanism of carrier localization in LVON, I analyzed temperature dependence of ρ , which suggested that the carrier localization was caused by disordered

potential introduced by randomly substituted nitrogen atoms. This conclusion indicates that the conductivity of perovskite-type oxynitride could be controlled by modulation of its potential.

One approach for enhancement of conductivity is stacking of undoped and doped layer. If the holes doped into oxynitride layer can penetrate into adjacent undoped layer, it is possible to reduce the influence of the disordered potential to the conduction of the material. This concept, referred to as “remote” doping, has been realized in oxide superlattice structures. Based on this idea, I tried remote hole doping from $\text{LaVO}_{3-x}\text{N}_x$ into LaVO_3 by fabricating superlattice structure of them.

$\text{LaVO}_3 / \text{LaVO}_{3-x}\text{N}_x$ single crystalline superlattice was epitaxially fabricated by applying NPA-PLD method. The oxide and oxynitride layers were alternately deposited with closing and opening the shutter attached in front of the nitrogen plasma source. X-ray diffraction (XRD) measurements revealed clear satellite peaks consistent with the periodicity of designed superlattices. Secondary ion mass spectroscopy (SIMS) confirmed periodic anion distribution, although a finite amount of nitrogen was detected in the oxide layer due to nitrogen leakage through the closed shutter. The conductance of the superlattice was higher than the sum of those of individual layers, suggesting contribution of remote doping. Remote doping was also supported by experiments on $\text{LaVO}_3 / \text{LaVO}_{3-x}\text{N}_x$ single heterostructure, which is relatively free from the effect of nitrogen leakage.

Another approach for enhancement of conductivity is reduction of randomness by forming ordered anion configuration. In case of ABO_2N -type perovskite oxynitrides, there are two local configurations, *cis*- and *trans*-type ones. In bulk oxynitrides, generally, complicated *cis*-network without long-range ordering is formed. If long-range ordering is established, random potential should be reduced. Based on the idea, I focused on topotactic nitridation of layered perovskite (LP) oxide. $\text{LP-La}_2\text{Ti}_2\text{O}_7$ can be nitrided into

perovskite-type LaTiO_2N with ammonolysis method, in which nitrogen substitution predominantly proceeds along the excess oxygen layers. Therefore, LnTiO_2N with long-range anion ordering might be obtained by nitrating LP- $\text{Ln}_2\text{Ti}_2\text{O}_7$ epitaxial thin films.

LP- $\text{La}_2\text{Ti}_2\text{O}_7$ and $\text{Sm}_2\text{Ti}_2\text{O}_7$ thin films were epitaxially grown on (110) planes of STO and LSAT substrates. XRD measurements showed (100)- and (010)-orientation for $\text{La}_2\text{Ti}_2\text{O}_7$ of which excess oxygen layers were parallel and perpendicular to the film surface, respectively, due to the lattice mismatch on each substrate. After the ammonolysis process (1000 °C, 1 hour), the LP- $\text{Ln}_2\text{Ti}_2\text{O}_7$ thin films were converted to perovskite-type LnTiO_2N while the substrates were not nitrated. This process, therefore, is expected as another route to fabricate single crystalline oxynitride thin film. However, their XRD patterns did not show any patterns corresponding to anion-ordered structure nor any dependence on the orientation of the precursor. This result indicates random substitution of nitrogen for oxygen, probably because high reaction temperature required for ammonolysis caused random nitrogen diffusion.

In conclusion, I revealed intrinsic transport properties of perovskite-type oxynitride and developed several ways toward control of its transport properties with the aid of epitaxial growth techniques. Resistivity measurements of $\text{LaVO}_{3-x}\text{N}_x$ thin films revealed strong carrier localization due to disordered potential originating from random substitution of nitrogen for oxygen. This indicates that modulation of the disordered potential would drastically change the transport properties of perovskite-type oxynitride. In this study, I challenged two approaches to reduce randomness in conduction path. Remote hole doping from oxynitride to adjacent oxide layer was performed with oxide/oxynitride stacked structures, and enhanced conductivity was observed. Topotactic nitridation of single-oriented LP oxide might be one route for fabricating anion-ordered structure, although this approach still needs further optimization of the reaction conditions to suppress thermal diffusion of N.

Acknowledgement

I would like to show my applications for those who kindly help me in this study. First of all, I appreciate my supervisor, Prof. Tetsuya Hasegawa. He provided me a lot of advices full of kindness and deep insight, wonderful experimental environment and precious opportunities such as Advanced Leading Graduate Course for Photon Science (ALPS) program and collaborative research. I am also grateful to Assoc. Prof. Yasushi Hirose, who regularly helped me with my research through kind and constructive advices.

I also owe my doctoral thesis to Prof. Tomoteru Fukumura, who gave me greatly beneficial advices for analysis of experimental results. The advices and comments by Dr. Akira Chikamatsu and Dr. Hideyuki Kamisaka helped me break the difficulty in this study. Mr. Shoichiro Nakao gave me a lot of knowledge and advices effective for the research.

I received generous supports in nuclear reaction analysis measurement from Prof. Katsuyuki Fukutani of the University of Tokyo and Assoc. Prof. Kimikazu Sasa, Mr. Satoshi Ishii and Dr. Daiichiro Sekiba of University of Tsukuba. Prof. Osamu Ishitani and Assoc. Prof. Kazuhiro Maeda of Tokyo Institute of Technology gave me a precious opportunity for ammonolysis reaction and a lot of advices full of insight. Mr. Takayoshi Oshima and Mr. Kanemichi Muraoka of Tokyo Institute of Technology kindly helped me conduct the reaction and gave a lot of beneficial advices. I also thank the members in Ishitani-Maeda laboratory of Tokyo Institute of Technology, who gave me a warm welcome.

I also would like to appreciate Prof. Shinichi Ohkoshi, the secondary advisor in ALPS program, for his warm comments to my study. I also thank ALPS program.

I would like to thank to the members of Hasegawa laboratory: Dr. Sohei Okazaki, Dr. Chang Yang, Dr. Daisuke Ogawa, Dr. Anri Watanabe, Dr. Youngok Park, Dr. Daichi Oka, Dr. Kei Shigematsu, Dr. Jie. Wei, Dr. Shungo Kojima, Dr. Tsukasa Katayama, Dr.

Thantip. S. Krasienapibal, Dr. Kenta Shimamoto, Dr. Atsushi Suzuki, Dr. Jeon Il, Ms. Xi Shen, Mr. Kazuki Aizawa, Mr. Shun Inoue, Dr. Mayuko Oka, Dr. Ryosuke Sei, Ms. Kaori Kurita, Mr. Ryosuke Takagi, Mr. Tomoya Onozuka, Mr. Kenichi Kaminaga, Mr. Jumpei Takahashi, Mr. Kyohei Yamatake, Mr. Vitchaphol Motaneeyachart, Mr. Keisuke Kawahara, Mr. Yuji Kurauchi, Mr. Ryota Kantake, Mr. Fahd S. Kahn, Mr. Yutaka Uchida, Mr. Dai Kutsuzawa, Mr. Takuma Takeda, Mr. Takanori Yamazaki, Mr. Shunsuke Shibata, Mr. Naoki Kashiwa, Mr. Naoaki Hashimoto, Mr. Keisuke Yamada, Mr. Toru Koizumi, Mr. Takaaki Shiina, Mr. Michitaka Fukumoto, Mr. Satoshi Fujiwara, Mr. Takahiro Maruyama, Ms. Zhu Yuting, Mr. Ruocheng Han, Mr. Shunya Tanaka, Mr. Ken Hayahara, Mr. Shishin Mo, Mr. Kuni Yamada, Mr. Takuto Wakasugi, Mr. Jin Gou, Mr. Gu Ke, Mr. Zhong Jiangnan, Mr. Ryosuke Ishigami, Mr. Takuya Sahashi, Mr. Masato Tsuchii and Mr. Kento Magara. I would also thank the secretaries. Mrs. Mie Umino, Mrs. Aya Imoji, Mrs. Mayuko Kikuchi and Mrs. Miki Komazawa.

Finally, I would like to show my gratitude to my family and friends for their warm encouragement and kind help.

Contents

Chapter 1 General introduction.....	1
1.1 Perovskite-type oxide.....	1
1.2 Perovskite-type oxynitride.....	9
1.3 Purpose of the study.....	13
Chapter 2 Experimental techniques.....	16
2.1 Pulsed laser deposition (PLD).....	16
2.2 X-ray diffraction (XRD).....	18
2.3 Reflection high energy electron diffraction (RHEED).....	22
2.4 Atomic force microscopy (AFM).....	24
2.5 Energy dispersive X-ray spectroscopy (EDX).....	24
2.6 Nuclear reaction analysis (NRA).....	25
2.7 Secondary ion mass spectroscopy (SIMS).....	26
2.8 Electric transport property measurement.....	27
Chapter 3 Intrinsic carrier transport properties in perovskite-type oxynitride $\text{LaVO}_{3-x}\text{N}_x$	30
3.1 Introduction.....	30
3.2 Experimental procedure.....	31
3.3 Results and discussion.....	31
3.4 Summary.....	45
Chapter 4 Formation of oxide/oxynitride superlattice for remote doping.....	46
4.1 Introduction.....	46
4.2 Experimental procedure.....	47
4.3 Results and discussion.....	48
4.4 Summary.....	56

Chapter 5 Topotactic nitridation of layered perovskite oxide for anion-ordered structure	58
5.1 Introduction.....	58
5.2 Experimental procedure.....	60
5.3 Results and discussion.....	60
5.4 Summary.....	65
Chapter 6 General conclusion.....	66
Appendix Chapter A Fabrication of perovskite-type oxynitride with large lattice distortion.....	69
A.1 Introduction.....	69
A.2 Experimental procedure.....	70
A.3 Results and discussion.....	70
A.4 Summary.....	72
Bibliography.....	75

Chapter 1

General introduction

1.1 Perovskite-type oxide

1.1.1 Perovskite-type structure

Perovskite-type oxide is one group of metal oxides with a general chemical formula of ABO_3 . Its unit structure is shown in Fig. 1.1. This structure is adopted by many oxides, and their crystal structure is predicted by Goldschmidt tolerance factor (t) [2], which is calculated from the ratio of the ionic radii as

$$t = (r_A + r_O) / \sqrt{2} (r_B + r_O) \quad (1.1)$$

where r_A , r_B and r_O are the ionic radii of A -site cation, B -site cation and oxide ion, respectively. In an ideal perovskite-type structure, $t = 1$. But actually, cubic structure is observed even if t is slightly smaller because of thermal vibration of the lattice. When the ionic radius of A -site cation is too small for its site (small t), the BO_6 octahedral tilts to reduce the size of A -site [3]. As far as the tilting is less significant, the crystal still has perovskite-type structure, with orthorhombic or monoclinic structure. If the tilting is not negligible, different crystal structure called ilmenite is formed. On the other hand, for large t (> 1), hexagonal variants are formed.

I also briefly introduce layered structures related to perovskite-type structure. There are several structures which include ABO_3 unit structure in common, such as layered perovskite (LP) phase ($A_nB_nO_{3n+2}$), Dion-Jacobson phase ($A'A_{k-1}B_kO_{3k+1}$) and Ruddlesden-Popper phase ($A_{j+1}B_jO_{3j+1}$) [4]. In these structures, the perovskite block with n , k or j BO_6 octahedra thick is alternately stacked with each other. Among these structures, LP phase has a characteristic structure that its perovskite unit makes 45° with

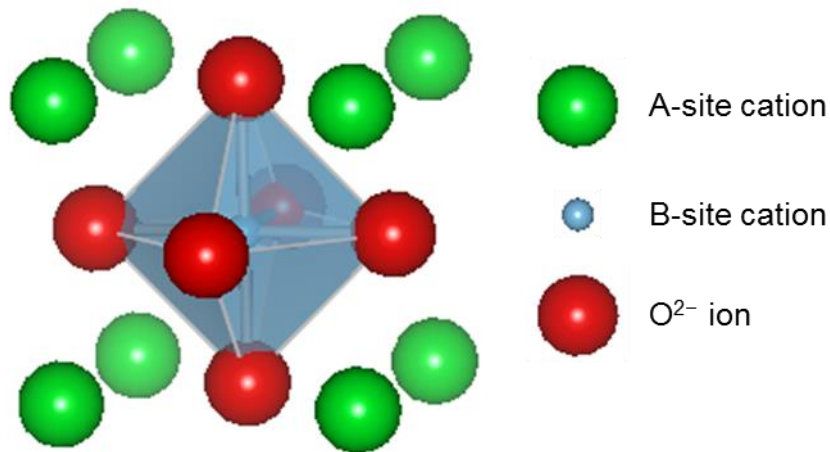


Figure 1.1 Schematic illustration of a perovskite-type structure. This structure was drawn with VESTA [1].

respect to the axis normal to its excess oxygen layers. The LP phase with $n = 4$ has the same chemical formula ($A_2B_2O_7$) as pyrochlore, and some materials can take both crystal structures [5]. The phase stability depends on the ionic radius of *A*-site cation: LP phase is favored by large *A*-site cations. For example, Bayart *et al.* reported the phase transition of $\text{La}_2\text{Ti}_2\text{O}_7$ from LP phase to pyrochlore phase by doping lanthanoid ion with a smaller ionic radius [6].

1.1.2 Transport properties of perovskite-type oxide

Since perovskite-type structure is robust against chemical doping, perovskite-type oxide has been intensively studied to develop new functionalities which are controllable by substitution of the cations. For example, modulation of optical bandgap, dielectric constant and magnetization has been performed for perovskite-type BiFeO_3 [7,8]. Among various physical properties, transport properties have attracted attention for applications in a field of electronic industry. In this section, I introduce several topics about transport properties of perovskite-type material.

Carrier transport properties of material are strongly affected by the shape of orbitals which contribute to the carrier conduction, because transfer integral increases as

the orbital overlap increases. For example, typical metal oxides, such as ZnO, have conduction bands consisting of isotropic metal s-orbitals. Therefore, their conductivity does not depend on the direction of the conduction, and is less influenced by lattice distortion. For this advantage, typical metal oxides are used for flexible devices. On the other hand, carrier transport in perovskite-type oxide is governed by the d band of transition metal ion and the $2p$ band of oxide ion. Since they are highly anisotropic, the conductivity of perovskite-type material is strongly affected by its crystal structure and crystallinity. It is well known that amorphous perovskite-type oxides show much higher resistivity than crystalized ones. In case of polycrystalline samples, transport properties are also affected by extrinsic factors, such as grain boundary, which work as scattering centers for carriers [9].

Understanding carrier conduction mechanism is important because it might give an idea how to control the transport properties. The conduction mechanism in semiconductors is mainly classified into two groups: band conduction and hopping conduction. Band conduction is observed in most of metal oxide semiconductors. In this conduction, carriers flow through particular bands. One example is a doped band insulator. When an element that has more valence electrons is doped, it forms a donor level just below the conduction band, and the electron in the donor level works as a carrier. Such an element is called n -type dopant. On the other hand, when an element that has less valence electrons is doped, it forms an acceptor level just above the valence band, and a hole in the acceptor level works as a carrier. Such an element is called p -type dopant. Another origin of carrier is thermal excitation. When thermal energy enough for electrons in the valence band to excite into the conduction band is added, a pair of electron and hole are formed, which work as carriers. This pair can recombine at a certain rate. Therefore, at constant temperature, thermal equilibrium with a constant carrier density is achieved. The temperature dependence of resistivity ρ obeys famous Arrhenius law

$$\rho(T) = \rho_0 \exp(-E_a / kT) \quad (1.2)$$

where E_a and k represent the activation energy and the Boltzmann constant, respectively.

In organic materials and disordered materials, band structure is not formed owing to their non-periodicity, and carriers are trapped at localized states. In such materials, carriers move by repeating hopping between localized states by thermal energy. This conduction is called hopping conduction. Because hopping needs thermal energy corresponding to the energy difference between the states, the hopping behaves differently depending on temperature. When temperature is high enough for carriers to hop into any sites, hopping to the nearest-neighbor sites is dominant, as illustrated in Fig. 1.2a. This conduction is called nearest-neighbor hopping (NNH) conduction. In this conduction, the probability of hopping to each site is almost independent with temperature, and the temperature dependence of ρ obeys Arrhenius relation (eq. (1.2)), similar to the band conduction. When temperature is low, the probability of hopping to each site is no longer constant. It decreases as the energy difference between the sites increases. In this case, hopping between sites with the same energy levels is dominant, as illustrated in Fig. 1.2b. This type of conduction is called variable range hopping (VRH) conduction. VRH has two types; Mott-VRH and Efros-Shrovsikii-VRH (ES-VRH). Mott-VRH is widely observed in organic semiconductors and doped Mott insulators. The temperature dependence of ρ in Mott-VRH depends on the dimension of the material, as

$$\rho(T) = \rho_0 \exp(-aT^{-1/(d+1)}) \quad (1.3)$$

where a is a constant and d is the dimensionality of the material ($= 1, 2, 3$). ES-VRH is observed when electron correlation is strong. Density of states (DOS) near the Fermi energy differs between Mott-VRH and ES-VRH models, as illustrated in Fig. 1.3. In disordered materials, carriers are confined in localized states. Without electron correlation, DOS is constant against energy E . On the other hand, when electron correlation is strong, Coulomb interaction destabilizes the energy level near the Fermi energy, and a soft gap

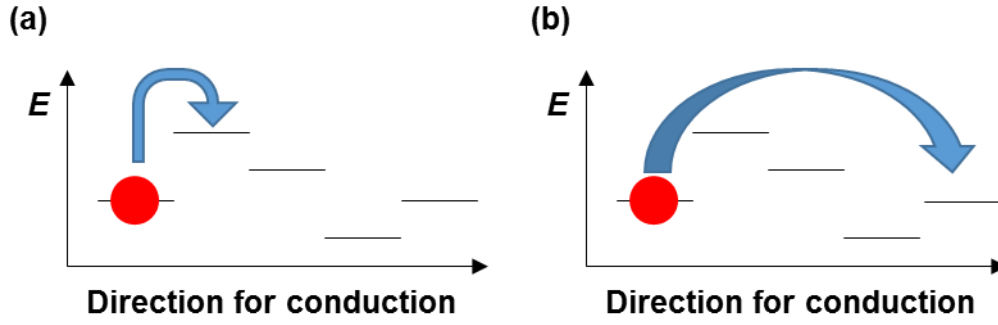


Figure 1.2 Schematic images of energy levels and hopping conduction: (a) Nearest-neighbor hopping and (b) Mott variable-range hopping.

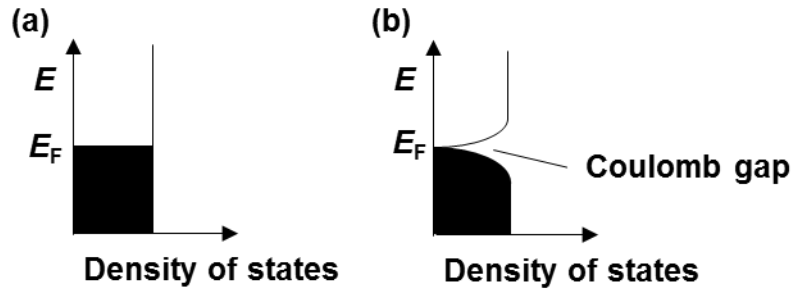


Figure 1.3 Schematic images of DOS for material showing (a) Mott-VRH and (b) ES-VRH.

called Coulomb gap is formed [10]. The difference in the shape of DOS results in the different temperature dependence of ρ ; in the case of ES-VRH,

$$\rho(T) = \rho_0 \exp(-aT^{-1/2}) \quad (1.4)$$

Since the contribution of Coulomb gap is easily hidden by thermally activated carriers, ES-VRH is observed at very low temperature, generally below 10 K.

Carrier doping by physical or chemical approaches changes the physical properties of perovskite-type oxide. Especially, drastic change of them has been reported for materials in which Coulomb interaction between valence electrons is strong. Such materials are called strongly correlated electron systems [11], and many perovskite-type oxides belong to this group. One example of strongly correlated electron system is Mott insulator. Mott insulator is a class of insulator which should show metallic conductivity based on the classical band theory by Wilson [12]. In Mott insulator, carriers are localized

owing to strong Coulomb repulsion between valence electrons [13], as illustrated in Fig. 1.4a. Each valence electron is localized on each ion. Mott insulator undergoes insulator to metal transition (IMT) through physical or chemical modification [14,15]. One approach for IMT is control of orbital overlap. Since carrier localization in Mott insulator is based on the balance between Coulomb repulsion and transfer integral, if the transfer integral exceeds the Coulomb repulsion, Mott insulator turns into metallic state. Larger orbital overlap increases the transfer integral, hence induces IMT, as illustrated in Fig. 1.4b. Orbital overlap can be modulated physically by applying pressure and chemically by doping, both of which deform the crystal lattice [16,17]. Indeed, IMT induced by the change of ionic radius in A-site has been reported [18,19]. Another approach is control of band filling. If the band filling deviates from the half-filled state, valence electrons can move between sites, as shown in Fig. 1.4c. Control of band filling has been realized by several methods. Physically, field effect is used to modulate band filling, and IMT with this approach has been reported [20]. Chemical substitution is another approach. One typical example is rare earth vanadate $ReVO_3$ [21], where replacement of trivalent Re^{3+} ion by divalent ion such as Sr^{2+} and Ca^{2+} decreases the band filling and induces IMT.

In a search of new functionality in perovskite-type oxides, there has recently been considerable interest in oxide heterostructures. Since Ohtomo *et al.* reported metallic conduction at the interface between $SrTiO_3$ and $LaAlO_3$ [22], oxide/oxide interface has been intensively studied for its unique transport properties different from the bulk state. For example, $LaTiO_3/SrTiO_3$ superlattice was found to show superconductivity [23] and nonlinear Hall effect [24]. The transport properties were revealed to depend on the thickness of individual layers [23]. From the measurement of the valence states of the metal ion, gradual distribution of the valence electron, which is quite different from the abrupt one of the ions, was observed [25]. The distribution is regarded as penetration of the carrier within ~ 2 nm, considered to be responsible for the peculiar transport properties.

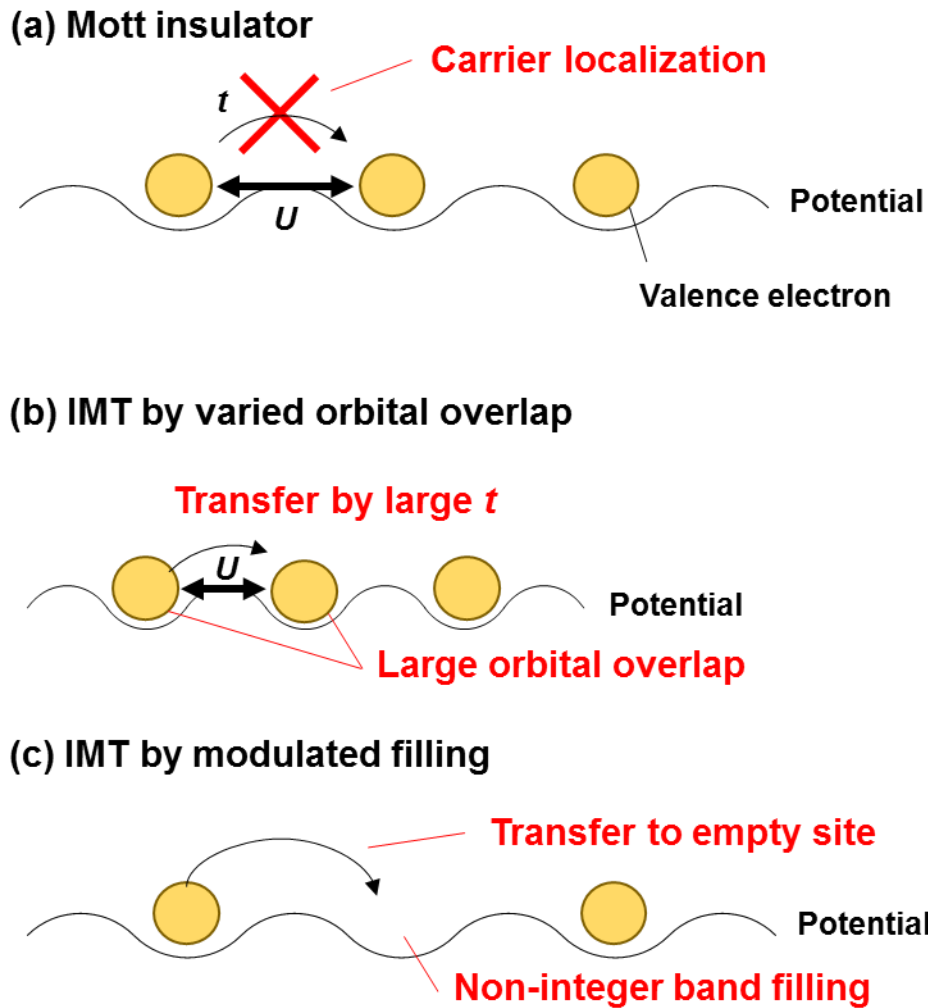


Figure 1.4 Schematic images of (a) Mott insulator, (b) IMT by varied orbital overlap and (c) IMT by modulated filling. U and t mean Coulomb repulsion and transfer integral, respectively.

Such penetration of charged carrier has already been used for GaAs-based field effect transistor [26,27]. GaAs shows electron mobility higher than Si and is useful for field effect transistor, while its mobility drastically reduces by impurity scattering. To achieve high mobility in GaAs-based devices, a technique of doping called modulation doping is used. One famous device using modulation doping is high electron mobility transistor (HEMT). HEMT has a junction between undoped GaAs and Si doped AlGaAs. Si works as an n-type dopant. As conduction band minimum of AlGaAs is higher than that of GaAs, doped electrons are accumulated near the interface between them in the

GaAs layer. Since electrons in GaAs are not scattered by dopant ions, HEMT can establish both high mobility and high carrier concentration.

1.1.3 Epitaxial growth

As perovskite-type oxides show wide variety of interesting physical properties, many perovskite-type materials have been intensively studied for new functionalities. For investigation of intrinsic physical properties, single crystalline sample is suited because polycrystalline sample shows physical properties which include extrinsic factors such as grain boundary.

As a synthetic technique for single crystals with high crystallinity, epitaxial growth has been used in a wide field. Figure 1.5 is schematic illustration of epitaxial growth. In epitaxial growth, a single crystalline thin film is deposited on a lattice-matched single crystalline substrate by using epitaxial force. If substrate and thin film are the same material, this situation is called homo-epitaxial growth. Homo-epitaxial growth is used to obtain high-quality single crystal. On the other hand, growth of a different material from substrate is called hetero-epitaxial growth. In hetero-epitaxial growth, the crystal structure and the lattice parameters of substrate strongly affect the crystallinity, crystal structure and physical properties of the thin film. It is preferable that substrate material has the same crystal structure as thin film. For this reason, thin layer of a material with the same crystal structure as objective is sometimes used as a buffer layer [28]. The tendency that the crystal structure of thin film reflects that of substrate, however, enables fabrication of thin film with metastable crystal structure. For example, $\text{Sm}_2\text{Ti}_2\text{O}_7$ and $\text{Gd}_2\text{Ti}_2\text{O}_7$ with metastable layered perovskite structure, which needs high pressure to synthesize in bulk [5], can be fabricated with use of lattice-matched substrates [29-31]. A parameter, lattice mismatch, helps appropriate selection of substrate for epitaxial growth. Lattice mismatch is defined as

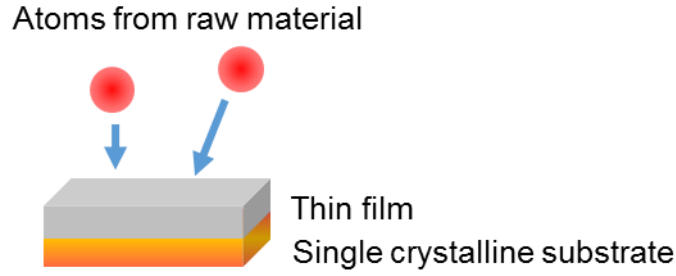


Figure 1.5 Schematic illustration of epitaxial growth.

$$\text{Lattice mismatch} = (a_{\text{film}} - a_{\text{subst}}) / a_{\text{subst}} \times 100 \quad (1.5)$$

where a_{film} and a_{subst} are the lattice parameters of the thin film and the substrate, respectively. In common, lattice mismatch below 2% is favored for epitaxial growth.

One key issue of epitaxial growth is lattice strain from substrate. The crystal lattice of film is sometimes distorted by the strain so that its in-plane lattice parameter becomes close to that of the substrate, while large lattice mismatch and large film thickness tend to relax the lattice. Applying lattice strain is one promising approach for achieving novel physical properties, because it can modulate orbital overlap and the distance between ions, which are often related to the physical properties. When lattice mismatch is small enough, the film has the same in-plane lattice parameter as the substrate. This growth mode is called coherent growth. In the case of coherent growth, the interface between the substrate and the film has no misfit transition, and the crystallinity of the thin film is generally good.

1.2 Perovskite-type oxynitride

1.2.1 Introduction of perovskite-type oxynitride

Substitution of metal element into perovskite-type oxide has been widely studied to realize novel functionalities. As a new approach, substitution of non-metal elements, such as N, F and H for O, has recently stimulated interest of researchers. For example, superconductivity was reported for $\text{Sr}_2\text{CuO}_2\text{F}_{2+\delta}$ [32], which contains perovskite-type unit

structure. Among them, perovskite-type oxynitride $ABO_{3-x}N_x$ has attracted much attention due to its optical properties associated with its unique band structure. Figure 1.6 schematically illustrates the band structures of oxide and oxynitride semiconductors. In typical oxide semiconductors, its valence band and conduction band mainly consist of O $2p$ and metal d band, respectively. When nitrogen is substituted for oxygen sites, its valence band maximum shifts upward due to nitrogen atom with small electronegativity. Therefore, the bandgap of oxynitride is generally small compared to that of oxide with the same cations and the crystal structure. Because of the small bandgap, oxynitride has been intensively studied as visible light active materials and pigments. For example, several oxynitrides were reported to work as catalysts for water splitting [33-35] in the coexistence of sacrificial reagents, although their efficiency is still small.

Recently, oxynitride has also attracted attention due to its electronic properties. One electronic feature of oxynitride is the strong metal-nitrogen bond originating from its strong bond covalency. Strong bond generally deforms the lattice and modulates its dielectric properties. For example, $SrTaO_2N$ is reported to show high dielectric constant and ferroelectricity [36]. Another feature of oxynitride is its electron configuration. Since oxynitride is regarded as doped oxide in which trivalent N^{3-} ion is substituted for divalent O^{2-} ion, it is considered as hole-doped system. Indeed, positive Seebeck coefficient, indicating p-type behavior, has been reported for several oxynitride semiconductors [37,38].

1.2.2 Crystal structure of perovskite-type oxynitride

Perovskite-type oxynitride has a chemical formula $ABO_{3-x}N_x$. One typical compound is ABO_2N ($x = 1$), and its structure has been intensively studied. Oxygen in perovskite-type oxide is described as a vertex of BO_6 octahedral. Based on this description, there are two kinds of nitrogen locations in ABO_2N , as shown in Fig. 1.7. They are called

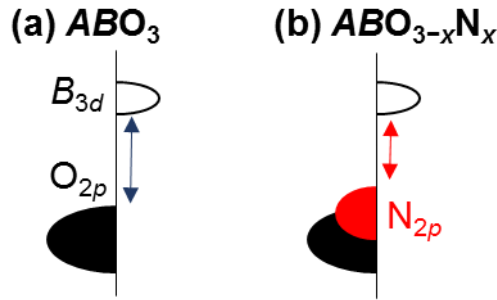


Figure 1.6 Schematic images of band structures of perovskite-type (a) ABO_3 and (b) ABO_2N .

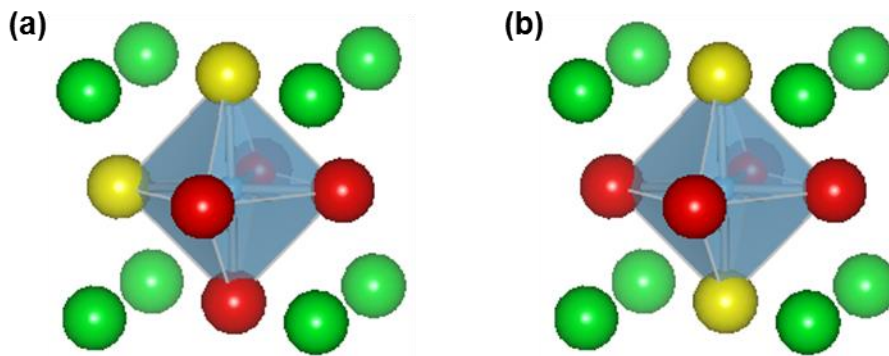


Figure 1.7 Schematic illustration of perovskite-type ABO_2N structures with (a) *cis*- and (b) *trans*-type local configuration. Red and yellow spheres represent O and N, respectively. These structures were drawn with VESTA [1].

cis- and *trans*- structures.

Determination of N position is difficult because O and N have small and similar atomic mass values. In case of mixed cation compound, cation ordering is relatively easily discernible from the satellite peaks in X-ray diffraction patterns [39]. On the other hand, determination of ordered structure is difficult for oxynitride because of similar atomic structural factors. One technique to determine N position is Rietveld refinement [40]. In this approach, precise crystal structure and local position of each atoms are estimated from its X-ray or neutron diffraction patterns using the models by least square method. Although this technique is a powerful tool for investigation of crystal structure, its use is limited for the following problems. First, this approach can be used only for samples with

polycrystalline powder form because it needs a number of diffraction peaks for calculation. Second, this method is not suitable for thin film samples because the intensity of diffraction peaks is weak. Therefore, determination of crystal structure for single crystalline thin film is still a hard task.

Rietveld refinement of bulk oxynitride revealed local *cis*-structure and 3D-zigzag arrangement of nitrogen [41,42]. It means that there is no long-range order in bulk state. Calculation of total energy for both structures also confirmed this tendency that perovskite-type oxynitride favors *cis*-type local configuration [36]. However, the calculation also predicted that *trans*-type local configuration may be energetically favored under strong biaxial compression which follows lattice distortion more than 2 %. Indeed, partial *trans*-ordering has been reported for strained $\text{Sr}_{1-x}\text{Ca}_x\text{TaO}_2\text{N}$ [43].

1.2.3 Synthesis methods of oxynitride

Oxynitrides have been synthesized in powder form so far. On the other hand, fabrication of single crystalline oxynitride is important for investigation of the transport properties. In this section, I introduce several methods for synthesis of oxynitride.

Conventionally, oxynitrides have been synthesized by ammonolysis method [44,45]. Figure 1.8 is schematic illustration of this method. In this method, an oxide precursor is heated over 500 °C in a flow of ammonia. At such high temperature, ammonia should dissociate into N_2 and H_2 completely, but the dissociation is suppressed in this condition owing to the equilibrium by residual N_2 and H_2 . Under such conditions, ammonia is highly unstable and drives the reaction. Although the detailed reaction mechanism has not been completely understood, H_2 is considered to pull out the oxygen atoms in the precursor.

However, ammonolysis method is not suitable to fabricate oxynitride to evaluate its transport properties, because it has the limitation for the form of sample. For uniform

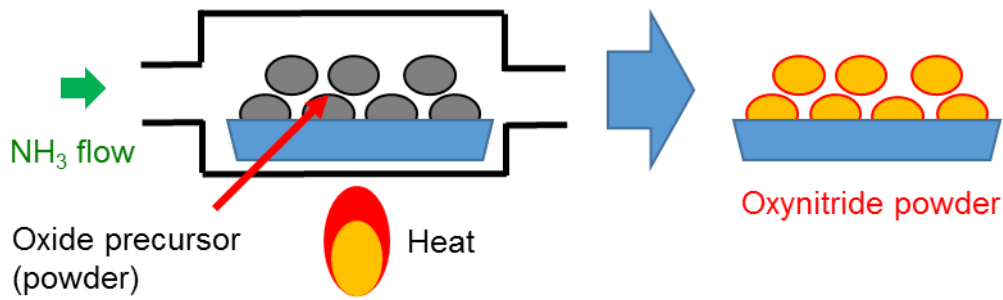


Figure 1.8 Schematic illustration of ammonolysis method.

nitridation, precursor oxide is generally in fine powder form. Moreover, single crystallization or sintering of the oxynitride is difficult, because oxynitride is generally decomposed into oxide at high temperature. Therefore, the observed transport properties of oxynitride synthesized by ammonolysis method include extrinsic contribution such as grain boundary effect [9,37].

Recently, several methods to synthesize oxynitride have been established. They are categorized into two types. The one is nitridation of an oxide precursor like ammonolysis method. For example, ion implantation using the ion beam can dope N into crystallized oxide [46]. Nitrogen plasma is also used for nitridation [47]. In these methods, however, distribution of N in depth direction is non-uniform and depends on the energy of the reactive species. The other is direct fabrication of oxynitride using epitaxial growth technique. Reactive species such as N radical [48,49] are used as N sources, while N_2 or NH_3 gas pulse was also recently used [50-52]. These methods would enable to fabricate single crystalline oxynitrides. Indeed, use of N radical in pulsed laser deposition method (NPA-PLD method) was reported to be effective for fabrication of perovskite-type oxynitrides [53]. However, reports on single crystalline oxynitrides are still rare, especially for oxynitride with non- d^0 configuration.

1.3 Purpose of the study

As mentioned above, intrinsic transport properties of perovskite-type oxynitride

have been rarely reported due to the limitation associated with the conventional synthesis method, ammonolysis. To overcome this problem, I focused on a different synthesis process called epitaxial growth. Single crystalline thin film can be grown by using epitaxial force from lattice-matched substrate. Since the starting material is once dissociated into atomic-scale species in this method, nitrogen can be introduced into the product by supplying activated nitrogen during deposition. Recently, fabrication of single crystalline oxynitride was reported [50,53], although most of the researches deal with d^0 -type oxynitride, not d^n -type one needed to investigate transport properties.

In this study, I aimed at fabrication of single crystalline oxynitride with non- d^0 configuration by nitrogen plasma assisted pulsed laser deposition (NPA-PLD) method. As a target material, I focused on a perovskite-type oxynitride $\text{LaVO}_{3-x}\text{N}_x$ (LVON). Its mother material LaVO_3 is a typical Mott insulator [54] and was reported to show IMT by substituting Sr [55,56] or Ca [57,58] for La. Because oxynitride is also hole-doped system, LVON is expected to show IMT. In contrast, LVON bulk polycrystal was reported not to show the transition [37,59]. This result suggests that LVON shows different electronic transport properties from La-site substituted compounds. However, the transport properties of LVON have been measured only for polycrystalline samples, and the specific electronic transport properties could not be identified as intrinsic ones.

As a first study, I fabricated LVON single crystalline thin film and analyzed its transport properties to investigate the intrinsic transport properties of perovskite-type oxynitride. As a result, I concluded that carrier localization due to randomly distributed nitrogen is an intrinsic feature of oxynitride.

Based on the information about the conduction mechanism mentioned above, I tried to control the electric transport properties from the following two points of view.

The first approach is focused on heterostructure. As mentioned in Section 1.1.2, heterostructure shows unique transport properties. One expectation for heterostructure is

carrier penetration into adjacent layer, which enables “remote” doping into undoped layer. Since undoped layer would show high mobility owing to the lack of dopant, heterostructure of doped and undoped layers may show enhanced carrier conduction compared to the sum of bulk conduction. Based on this idea, I fabricated superlattice and single heterostructure composed of LaVO_3 and $\text{LaVO}_{3-x}\text{N}_x$. Contribution of remote doping was investigated by comparing their conductance with those of single LaVO_3 and $\text{LaVO}_{3-x}\text{N}_x$.

The second approach is based on the directional reaction, as follows. Some LP oxides are known to be converted to perovskite-type oxynitride by ammonolysis process [60,61]. In this reaction, it is expected that nitrogen substitution predominantly proceeds along the excess oxygen layers in LP structure [60]. Since the layers make 45° with respect to the perovskite unit in it as mentioned in Section 1.1.1, it is expected that substituted nitrogen arranges for $\langle 110 \rangle$ direction of perovskite-type structure in the produced oxynitride. Therefore, by using LP epitaxial thin film as a precursor, long-range *cis*-arrangement might be realized. Based on the idea, an attempted was made to achieve ordered anion arrangement.

I was also engaged on the fabrication of perovskite-type oxynitrides with tetragonal strain with use of epitaxial strain toward trans-arrangement of nitrogen in oxynitride thin films.

Chapter 2

Experimental techniques

2.1 Pulsed laser deposition (PLD)

PLD is one of physical vapor deposition methods and used to fabricate thin film samples. In PLD method, high energy pulsed laser is focused on the starting material, called target, in high vacuum. Ablated target produces a plasma plume, and species in the plume are deposited on a surface of the substrate set just above the target. The merits of PLD in thin film synthesis are as follows:

- Fabrication of the sample at a temperature below the melting point of the material is possible, which enables wide growth conditions.
- PLD is a non-equilibrium process, and synthesis of metastable phases is possible.
- Synthesis of single crystal is possible with use of epitaxial growth technique.
- The crystal lattice distorts with use of proper substrate by epitaxial strain, which may give rise to new physical properties.
- Wide variety of materials such as oxides, metals [62] and nitrides [63] can be used as a target.
- The starting material need not be in liquid nor gas phases, which enables high purity in the fabricated thin films.
- Combinatorial fabrication is possible by alternating deposition with multiple kinds of targets. This technique can be applied to fabrication of stacked structure or solid solution with an arbitrary composition.
- The ratio of cations in the thin film is generally almost transferred from that of

the target, which enables easy modulation of the composition in the fabricated thin film.

For these merits, PLD is suitable to fabricate novel materials and to investigate their physical properties. Therefore, this method is widely used in laboratories. On the other hand, this method is not suitable for industrial use, because uniform deposition area is limited to at most $1\text{ cm} \times 1\text{ cm}$. For mass production, different methods such as sputtering are used.

Figure 2.1 shows schematic illustration of PLD method. In this study, a KrF excimer laser ($\lambda = 248\text{ nm}$) was used as a source of pulsed laser. A substrate was attached onto a graphite plate with metal paste, which was heated with an infrared lamp. The temperature of the plate was monitored with a pyrometer which measures radiation from the platinum paste spread on the plate. As a target, a ceramic oxide pellet, which has the same cation ratio as the objective, was generally used. On the other hand, an off-stoichiometric target is sometimes used when one of the elements in the target is highly

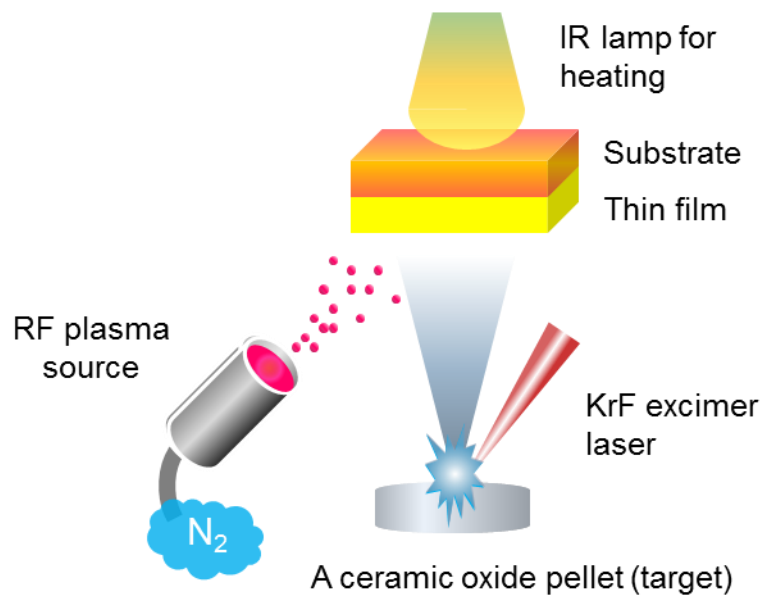


Figure 2.1 Schematic illustration of NPA-PLD method.

volatile, such as Bi. Atmosphere inside the chamber strongly affects the quality of deposited films. If molecules inside the chamber collides with the plume, the energy distribution of the plume is changed. Moreover, molecules might be incorporated into the film as impurities. To avoid these situations, the chamber was evacuated to UHV ($< 5 \times 10^{-8}$ Torr), and high purity gases suitable for the fabrication were supplied. Energy density and repetition rate of the laser were controlled by laser attenuators and a laser chopper, respectively. They determine the amounts of species in the pulsed plume and thus the growth rate of the thin film. Moreover, laser energy density determines the energy of species that reach to substrate, while laser repetition rate affects the time for species to migrate [64]. Therefore, energy density and repetition rate give a large influence on defect density and crystallinity, which frequently govern the physical properties of the thin film.

In this study, I combined a nitrogen plasma source with PLD for fabrication of oxynitride thin films. This method is called nitrogen plasma assisted PLD (NPA-PLD) [53,65,66]. As a nitrogen plasma source, radio frequency (RF) plasma (SVT Associates, Model 4.5”) was used. The RF source can generate nitrogen plasma by cutting the triple-bonds of N_2 molecules. The activated nitrogen was irradiated on the thin film during film fabrication. The activated nitrogen easily reacts with other species containing cation and oxygen in the PLD plume, and oxynitride thin film is fabricated.

2.2 X-ray diffraction (XRD)

X-ray is a part of electromagnetic wave, and its wavelength is in the range of 1pm-10nm. Since this wavelength range is comparable with or shorter than the period of crystal lattice, X-ray irradiated on a crystallized sample is diffracted when so-called Bragg’s condition is satisfied. Thus, the X-ray diffraction pattern is characteristic to the crystal structure of the sample. XRD was now widely used for determination of crystal structures. The relationship between diffraction angle and crystal structure can be

described by Laue condition and Bragg's law. Laue condition regards a crystal as a group of regularly arranged ions, while Bragg's law regards it as a group of planes with a constant interval. Therefore, Bragg's law can be considered as a specialized representation of Laue condition for a particular lattice plane.

Laue condition is based on the condition for scattered plane waves to interfere constructively. When an incident X-ray with wavevector \mathbf{k} is scattered by two ions separated by \mathbf{d} , and the diffracted ray has wavevector of \mathbf{k}' , the path difference between the rays must be an integer multiple of the wavelength. This condition is written as

$$\exp(i(\mathbf{k} - \mathbf{k}') \cdot \mathbf{d}) = 1 \quad (2.1)$$

In case of crystals, the position of ion \mathbf{R} is given by

$$\mathbf{R} = m_1\mathbf{a}_1 + m_2\mathbf{a}_2 + m_3\mathbf{a}_3 \quad (m_i: \text{integer}) \quad (2.2)$$

Substituting \mathbf{R} for d , diffraction condition is deduced as

$$\Delta\mathbf{k} \cdot (m_1\mathbf{a}_1 + m_2\mathbf{a}_2 + m_3\mathbf{a}_3) = 2\pi n \quad (n: \text{integer}) \quad (2.3)$$

where $\Delta\mathbf{k} = \mathbf{k} - \mathbf{k}'$. Because $\{\mathbf{a}_i\}$ are linearly independent, this condition is equivalent to the following conditions

$$\Delta\mathbf{k} \cdot \mathbf{a}_1 = 2\pi h; \Delta\mathbf{k} \cdot \mathbf{a}_2 = 2\pi k; \Delta\mathbf{k} \cdot \mathbf{a}_3 = 2\pi l \quad (2.4)$$

where h, k , and l are integers. These three conditions are called Laue condition. A group of $\Delta\mathbf{k}$ which satisfies Laue condition, $\{\mathbf{K}\}$, can be represented as

$$\mathbf{K} = h\mathbf{b}_1 + k\mathbf{b}_2 + l\mathbf{b}_3 \quad (h, k, l: \text{integer}) \quad (2.5)$$

with definition of $\{\mathbf{b}_i\}$ as

$$\begin{aligned} \mathbf{b}_1 &= 2\pi (\mathbf{a}_2 \times \mathbf{a}_3) / \{\mathbf{a}_1 \cdot (\mathbf{a}_2 \times \mathbf{a}_3)\} \\ \mathbf{b}_2 &= 2\pi (\mathbf{a}_3 \times \mathbf{a}_1) / \{\mathbf{a}_1 \cdot (\mathbf{a}_2 \times \mathbf{a}_3)\} \\ \mathbf{b}_3 &= 2\pi (\mathbf{a}_1 \times \mathbf{a}_2) / \{\mathbf{a}_1 \cdot (\mathbf{a}_2 \times \mathbf{a}_3)\} \end{aligned} \quad (2.6)$$

since $\{\mathbf{b}_i\}$ apparently satisfy Laue condition and are linearly independent. The space described by the vectors $\{\mathbf{b}_i\}$ as primitive vectors is called reciprocal lattice space, and \mathbf{K} is called reciprocal lattice vector. The name 'reciprocal' is based on the fact that $\{\mathbf{a}_i\}$ and

$\{\mathbf{b}_i\}$ are connected through Fourier transformation. With use of the concept of reciprocal space vector, arbitrary diffraction can be identified with three values h, k, l . They are called Miller indices and used to determine specific diffraction and the plane associated with the diffraction.

Bragg's law regards crystal lattice as a group of planes separated by an interplanar distance d . For constructive interference, the phase of the wave scattered from each plane must be equal. Therefore, Bragg's condition is deduced as

$$2d\sin\theta = n\lambda \quad (n: \text{integer}) \quad (2.7)$$

where θ is the diffraction angle, and λ is the wavelength of incident X-ray. Therefore, the observed diffraction angles give information about d in the sample. The obtained d values help to determine the crystal structure of the sample. Bragg's law can be also deduced from Laue condition as follows. In Bragg's law, \mathbf{a}_i corresponds to the vector normal to the diffraction plane. Therefore, Laue condition (Eq. 2.4) yields

$$2|\mathbf{k}| \cdot d \cos\phi = 2\pi m \quad (2.8)$$

where ϕ is the angle between \mathbf{k} and \mathbf{k}' . Since $k = 2\pi / \lambda$ and $\phi = 90^\circ - \theta$, Eq. (2.8) can be written as

$$2d \sin\theta / \lambda = m \quad (2.9)$$

which is equivalent to Bragg's law.

In this study, XRD was observed by Bruker's D8 DISCOVER. Figure 2.2 shows schematic illustration of the set-up. This equipment consists of three parts: an X-ray generator, a sample stage and a detector of diffracted X-ray. As an X-ray source, Cu K α line ($\lambda = 0.15418$ nm) was used. The generated X-ray was collimated and then irradiated on the sample. The sample stage was freely rotated in a three-dimensional manner, and the position of the detector against the incident X-ray was changed as shown in Fig. 2.2. As an X-ray detector, three kinds of detectors, 0D (scintillation counter), 1D and 2D detectors were used. 1D and 2D detectors were used for continuous ω - 2θ scan. 2D

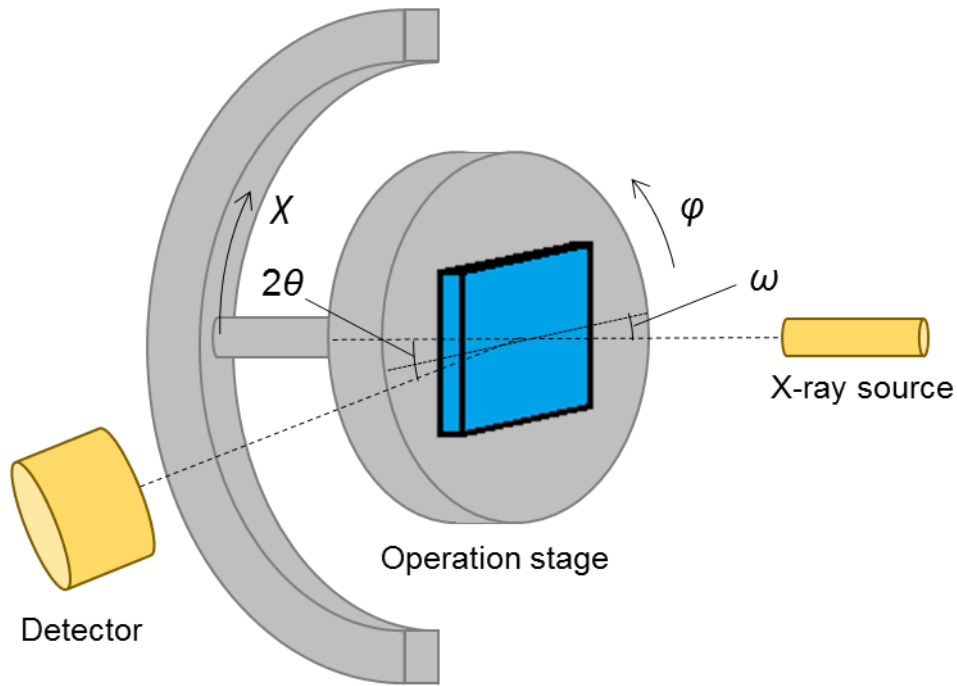


Figure 2.2 Schematic illustration of XRD setup.

detector can record χ dependence of signal and is effective to evaluate the crystallinity and the orientation of the sample. On the other hand, resolution of the diffraction pattern is higher in 1D detector than in 2D detector. 1D detector was also used to measure reciprocal space maps, which will be explained in the following paragraph. 0D detector has even higher resolution than the others, and it was used when measuring very weak pattern, rocking curve and interference fringe.

One application of XRD is reciprocal space mapping (RSM). This technique visualizes the reciprocal lattice plane from a series of 2θ - θ scans with different ω and can determine the components of the reciprocal lattice vectors. Since lattice constants of a crystal are related to its reciprocal lattice vectors, RSM is a powerful technique to determine lattice parameters. For example, the component of reciprocal lattice vector q_i ($i = 1, 2, 3$) in orthorhombic crystal can be converted to the length of corresponding lattice vectors a_i with the following simple relation

$$a_i = 1 / q_i \quad (2.10)$$

Since diffraction not only from thin film but also from substrate appears in a reciprocal space map, RSM is useful especially to determine whether the thin film lattice was grown coherently or relaxed.

2.3 Reflection high energy electron diffraction (RHEED) ^[67]

As electron beam can be regarded as a wave with the wavelength of $\lambda = h / p$ (de Broglie wave), where p is the momentum, an electron beam of which the wavelength is the same order as lattice constants shows diffraction similarly to X-ray. RHEED is a tool to observe crystal structure by scattering pattern of electron beam. Compared to X-ray, a beam of charged electrons strongly interacts with the electrons in solids. Moreover, the incident angle of the electron beam for RHEED is small. Therefore, its penetration depth is only several atomic layers. Because of this, RHEED is effective to observe the crystal structure at the surface. Another advantage of RHEED is its simple set-up. The incident angle of electron beam is so small that the components of RHEED, an electron gun and a fluorescence screen for visualization of the diffraction pattern, do not disturb thin film growth, which enables in-situ RHEED observation of thin film growth.

Several kinds of RHEED patterns appear depending on states of sample surface. The RHEED pattern can be understood by Ewald construction. This construction can visualize the conditions at which diffraction takes place based on the restriction of the wavevector \mathbf{k}' . Here, we restrict ourselves to elastic scattering, $|\mathbf{k}| = |\mathbf{k}'|$. Therefore, when two vectors \mathbf{k} and \mathbf{k}' are drawn from the common origin, the end points of \mathbf{k} and \mathbf{k}' must lie on a sphere of radius $|\mathbf{k}|$ centered at the origin. This sphere is called Ewald sphere. Because Laue condition states that the scattering vector $\mathbf{k} - \mathbf{k}'$ must be equal to reciprocal lattice vector, the end point of \mathbf{k}' must lie also on the reciprocal lattice whose origin is the end point of \mathbf{k} . Therefore, diffraction occurs when \mathbf{k}' lies at the intersection between the Ewald sphere and the reciprocal lattice. The shape of the intersection gives the shape of

diffraction pattern.

In an ideal single crystal with a flat surface, atoms are arranged equidistantly on a line along the incident beam. A reciprocal lattice of the atoms is a series of equidistant planes perpendicular to the line. Therefore, the intersection consists of circles with same center. This circular diffraction patterns are called Laue zones. In case of crystal with square lattice, atoms are arranged not only along the beam but also across it. Therefore, the reciprocal lattice for such crystal is a set of rod, and corresponding diffraction pattern displays spots located on the Laue zones.

In most cases, samples are not ideal owing to their small domains and rough surfaces. Such imperfect crystal structures have reciprocal lattice planes with finite width. Thus, the intersection, which corresponds to the diffraction pattern, is no longer spots but rods. Such a pattern is called streak pattern. If the surface is highly rough enough for electron beam to cause transmission diffraction, regular spots are observed similar to XRD. I also note that polycrystalline samples show ring patterns, in the same manner as X-ray diffraction.

One application of RHEED is observation of crystal growth mode. There are three kinds of growth modes for thin films: Frank-van der Merwe mode, Stranski-Krastanov mode and Volmer-Weber mode. In Frank-van der Merwe mode, an atomic layer is grown, followed by the next layer (2D growth). On the other hand, Stranski-Krastanov mode is an island growth mode or 3D growth mode. Volmer-Weber mode lies midway between the other two, and in this mode growth-type changes from 2D to 3D. In the case of Stranski-Krastanov mode, the intensity of diffraction pattern monotonically decreases with time, reflecting increase of surface roughness of the film. If the surface roughness is too large, diffraction pattern changes to regular spots as I mentioned before. On the other hand, in the case of Frank-van der Merwe mode, surface roughness is minimized when an atomic layer is completely formed, while it is maximized when half

of atomic layer is deposited. In this growth mode, therefore, the intensity of diffraction patterns oscillates, which is called RHEED oscillation. The period of the oscillation corresponds to the time for the growth of one atomic layer, and thus it is possible to directly evaluate the growth rate from the oscillation period.

2.4 Atomic force microscopy (AFM)

AFM is a kind of scanning probe microscopy and provides information about surface morphology of samples with atomic resolution. It measures the height of sample surface, detecting atomic force between sample surface and scanning probe attached at the end of a cantilever. On scanning, the cantilever bends according to the atomic force, and the amount of bending depends on the sample-probe distance. The bending is detected from dislocation of the reflected laser beam irradiated on the back-side of the cantilever. Then, the height of the cantilever is adjusted so as to keep the amount of bending constant, and information about the surface roughness is recorded. With this procedure, the surface morphology is imaged. In this study, a commercial scanning probe microscopy system (SII-nanotechnology, SPI4000 with SPA400) was used.

2.5 Energy dispersive X-ray spectroscopy (EDX)

EDX spectroscopy is one method for composition analysis. It detects characteristic X-ray emitted by incident electron beam. When electron beam whose energy is above the binding energy of electrons in inner shell is irradiated, electrons are ejected from the inner orbitals, and vacancy energy level is formed. Then, electrons in outer shell fall into the level for higher stability, and, at the same time, X-ray of which the energy is the same as the difference in energy between the outer and inner shells is emitted. Since the energy levels are characteristic of each element, the energy of emitted X-ray is also characteristic of it, called characteristic X-ray. Because characteristic X-ray of many

elements can be measured simultaneously by an energy-dispersive spectrometer, semi-quantitative composition analysis is possible.

EDX spectroscopy is a powerful tool for composition analysis, while it needs to pay attention to measurement conditions when used for thin film samples. Since emitted X-rays are less attenuated by sample than the incident electron beam, a measurement depth of EDX depends on the penetration depth of incident electron beam. The penetration depth of electron beam with 10 kV (the energy generally selected for quantitative analysis) for metal oxide is the order of sub-micrometer. Since this value is much larger than the usual film thickness, the measured spectrum includes the signal from substrate. If the thin film and the substrate contain the same element, it is hard to distinguish the signals from thin film and substrate. Even if the element of interest is contained only in thin film, quantitative analysis is not so easy because the sensitivity of each element depends on the film thickness.

Taking the above-mentioned cautions into consideration, I set the energy of electron beam enough low to prevent the electron beam from reaching to substrate. However, the analyzed composition data still had large uncertainty due to peak overlap; some characteristic X-rays have very close energy (e.g. $O_{K\alpha}$ line of 0.525 keV and $V_{L\alpha}$ line of 0.511keV), and their peaks are hard to separate. Because of this problem, I measured the compositions of several samples using resonance nuclear reaction analysis, to be mentioned in the next section, and used the samples as standard references for EDX measurements.

2.6 Nuclear reaction analysis (NRA)

As EDX has a problem for quantitative measurement of thin films, I used NRA as a more reliable method to determine nitrogen content. NRA uses nuclear reaction for elemental analysis. For nitrogen, the following reaction was used.



This reaction means that reaction of ^{15}N with proton produces ^{12}C with emission of α -ray and γ -ray. The energy of emitted γ -ray is specific to the reaction. Therefore, by counting the number of the γ -ray photons, nitrogen density in the sample is measured. As the natural abundance of ^{15}N is only 0.4%, resonance condition at 898 keV was used for high counting efficiency (Resonance NRA). In this study, NRA measurements were conducted with a 1-MV tandetron accelerator at Tandem Accelerator Complex, University of Tsukuba. The γ -ray was detected with two 3-inch $\text{Bi}_4\text{Ge}_3\text{O}_{12}$ scintillation counters. Nitrogen amount was calculated by comparing the peak intensity with that of the reference TiN thin film.

2.7 Secondary ion mass spectroscopy (SIMS)

SIMS is one of standard methods for composition analysis with the lowest detection limit (the order of ppb). This technique detects secondary ions ejected from the sample by irradiating ion beam. As a primary ion source, O^{2+} or Cs^+ is commonly used. O^{2+} and Cs^+ ions are used to detect positive and negative secondary ions, respectively, for high generation probability of the secondary ions. In this study, Cs^+ ion was used, because oxygen ion beam might oxidize the sample. The secondary ions are separated according to their masses and charges by a quadrupole mass analyzer. The analyzer consists of four parallel metal rods, and a radio frequency voltage with a direct current offset voltage is applied between them. When charged particles travel along the rods, the particle with a specific m/z ratio (m : mass, z : charge), which depends on the voltage applied to the rods, can only reach to the end while other particles collide with the rods. Therefore, a specific ion selectively reaches to the detector. By counting the number of each secondary ion, quantitative analysis is possible. Since the sensitivity is different between elements, calibration by using a standard sample is necessary for quantitative analysis. Standard

sample should be composed of the same elements and have the same crystal structure as the sample to minimize the matrix effect.

As SIMS requires sputtering of the sample, it is categorized as destructive analysis method. This shortage, however, enables depth profile analysis of the sample by continuous sputtering and detection processes. This technique is called dynamic SIMS.

2.8 Electric transport property measurement

In this study, electrical resistivity was measured by 4-probe method. In this method, two electrodes are used for flowing current, and the other two are for measuring voltage. Since the voltmeter has very high impedance, almost no current flows between the voltmeter and the electrode for voltage measurement. Thus, voltage drop at the electrodes is negligible. This method is useful for measuring low resistance samples. On the other hand, attention should be paid to highly resistive samples, in which current flowing the voltmeter is not negligible.

Figure 2.3 illustrates the set-up for 4-probe method. I used two kinds of set-up: simple 4-probe geometry and special one called van der Pauw method. For simple 4-probe geometry, a Ti mask plate was placed on substrate during fabrication in order to fabricate patterned samples as illustrated in Fig. 2.3a. A Patterned sample is suitable to measure resistivity with high precision while the use of mask plate has some demerits. First, the mask affects temperature distribution on the sample surface during the deposition, which is sometimes responsible for non-uniformity of the film. Second, the use of mask plate prevents RHEED measurement which gives important information about deposition rate. Taking these problems into consideration, some samples were fabricated without the mask and measured with the geometry illustrated in Fig. 2.3b.

Van der Pauw method can measure resistivity of thin film samples with arbitrary shape theoretically. In this method, 4 electrodes are placed at the corners of the sample,

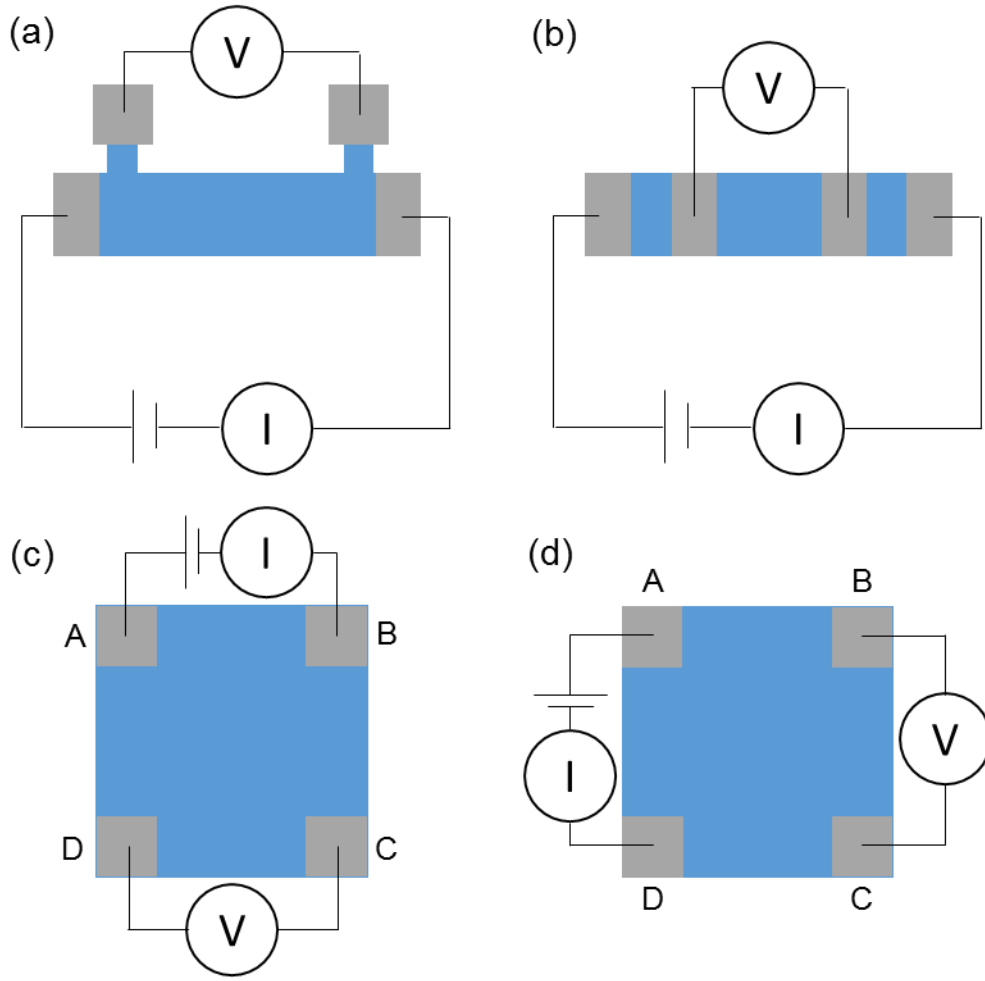


Figure 2.3 Schematic illustration of set-up for 4-probe method. (a) Simple 4-probe method for patterned sample (b) Simple 4-probe method for rectangle sample (c,d) Van der Pauw method with two geometry.

and 4-probe measurement is performed with two geometry. In the geometry illustrated in Fig. 2.3c, DC electric current flows between electrodes A and B, and the current between them (I_{AB}) and voltage drop between electrodes C and D (V_{CD}) are measured. Similarly, I_{AD} and V_{BC} are measured in the geometry illustrated in Fig. 2.3d. The resistivity ρ is given by following equation;

$$\rho = \{\pi d / \text{Ln}(2)\} \{(R_{AB,CD} + R_{BC,DA}) / 2\} f(R_{AB,CD} / R_{BC,DA}) \quad (2.12)$$

where $R_{AB,CD} = V_{CD} / I_{AB}$, $R_{AD,BC} = V_{BC} / I_{AD}$, d is the thickness of the thin film sample and f is the correction factor that accounts for the effects of non-ideal features of

experiments, such as the shape of the sample and the positions of electrodes.

In this study, resistivity was measured in a temperature range of 2-300K using a physical property measurement system (Quantum Design, model 6000).

Chapter 3

Intrinsic carrier transport properties in perovskite-type oxynitride $\text{LaVO}_{3-x}\text{N}_x$ *

3.1 Introduction

In this chapter, I report the intrinsic electrical transport properties of a perovskite-type oxynitride $\text{LaVO}_{3-x}\text{N}_x$ (LVON). LVON is expected to show specific electronic transport properties different from La-site substituted compounds [37,59] while extrinsic contribution such as grain boundary could not be excluded. For evaluation of the intrinsic electrical transport properties, I fabricated a series of LVON single crystalline thin films with different nitrogen amounts by NPA-PLD method. The qualities of the obtained films were evaluated from their crystal structure and surface morphology. The electrical transport properties of the LVON thin films were measured and compared with previous reports. Finally, intrinsic transport properties of LVON and its origin were discussed.

* This chapter contains the contents of the following publication.

1) M. Sano, Y. Hirose, S. Nakao and T. Hasegawa, *J. Mater. Chem. C* **5**, 1798 (2017).

3.2 Experimental procedure

LaVO_{3-x}N_x thin films were epitaxially grown on (100) planes of SrTiO₃ (STO) (Shinkosha Co., Ltd.) and (La_{0.3}Sr_{0.7})-(Al_{0.65}Ta_{0.35})O₃ (LSAT) (CrysTec GmbH) substrates by NPA-PLD method. A LaVO₄ ceramic target was used as a target. The target was synthesized by solid state reaction of La₂O₃ powder (99.99% purity) and V₂O₅ powder (99% purity) at 600 °C for 24 hours, followed by sintering at 700 °C for 72 hours. The depositions were conducted under N₂ gas pressure of 1 × 10⁻⁵ Torr, and the N₂ gas was activated by RF plasma source (SVT Associates, Model 4.5”). The repetition rate of the pulsed laser was fixed at 4 Hz. The nitrogen content was controlled by input power of RF source (0-400 W) and laser energy (5.4-8.0mJ).

Crystal structures of the thin films were determined by XRD and RHEED. The thickness was measured with a stylus profiler (VEECO, Dektak 6M). The composition was evaluated by EDX. For precise quantitative analysis of nitrogen content, NRA was also performed. Surface morphologies were observed by AFM. Electrical resistivity was measured for patterned LVONs by 4-probe method with Au electrode.

3.3 Results and discussion

3.3.1 Synthesis of LaVO_{3-x}N_x epitaxial thin films

Perovskite-type LVON thin films were grown by NPA-PLD method. First, I optimized substrate temperature (T_S), which strongly affects the crystal structure and crystallinity of grown thin films. Figure 3.1a compares $\theta - 2\theta$ XRD patterns of the LVON thin films grown on LSAT (100) substrates at various T_S . The films grown at $T_S \geq 500$ °C showed strong diffractions near $2\theta = 22.3^\circ$ and 45.5° , which match 100 and 200 reflection of the perovskite-type structure, respectively. They strongly indicate growth of (100)-oriented LVON. On the other hand, the films grown at $T_S = 450$ °C showed much weaker diffractions, and no diffraction was observed for the films grown at $T_S = 400$ °C. This

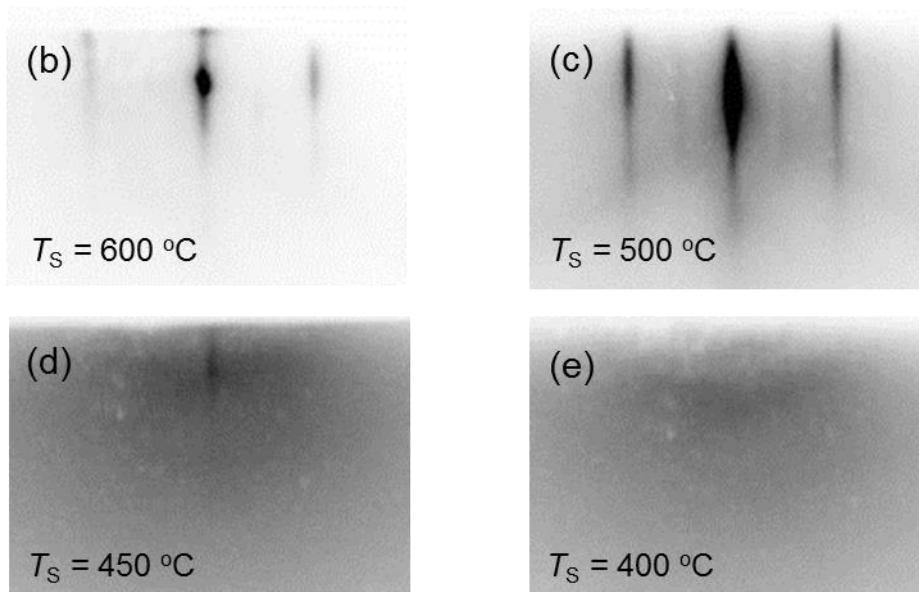
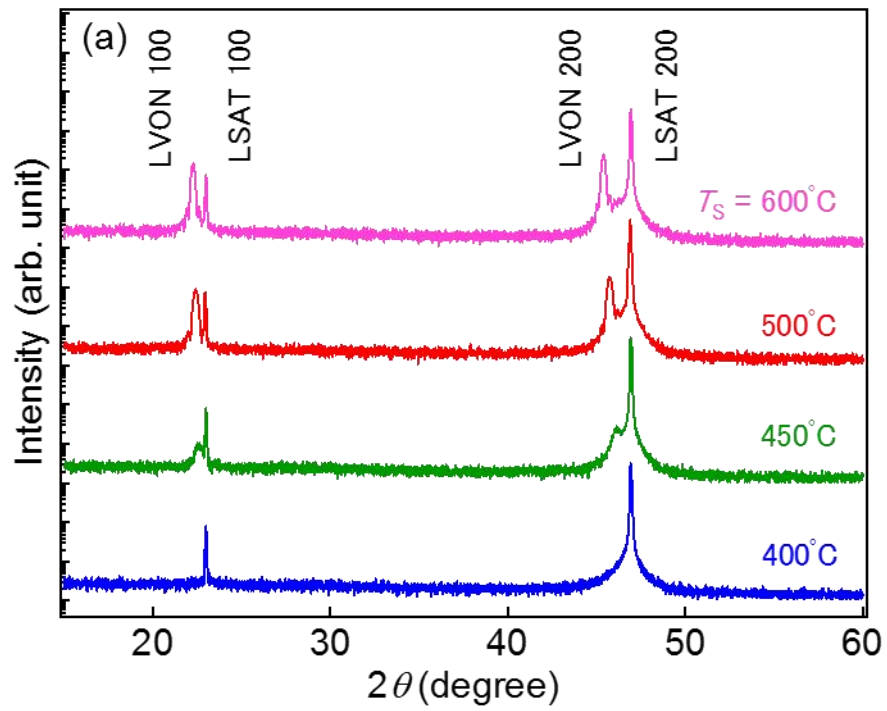


Figure 3.1 (a) XRD patterns and (b-e) RHEED patterns of the LVON thin films grown on LSAT (100) substrates at various T_S .

result indicates that at least 500 °C is necessary to grow LVON with high crystallinity.

The crystallinity of the thin films was also reflected in their RHEED patterns (Fig. 3.1b-e). The films grown at $T_S \geq 500$ °C showed apparent streak pattern, indicating formation of single crystal. The films grown at $T_S = 450$ °C showed faint streak pattern, suggesting partially amorphous structure. The films grown at $T_S = 400$ °C showed no pattern reflecting its amorphous structure.

Figure 3.2a shows EDX spectra of the films. Acceleration voltage of electron beam was set at 1.5 keV so that signals from the substrate was not included in the spectra. There were five peaks. Peaks at 0.27 keV originate from C in organic impurities at the surface of the films. Peaks at 0.63 keV and 0.84 keV correspond to La_{Mz} and $La_{M\alpha}$ lines respectively. Peaks around 0.39 keV and 0.52 keV are mainly $N_{K\alpha}$ (392 eV) and $O_{K\alpha}$ (525 eV) lines, although peaks of V (V_{Ll} and $V_{L\alpha}$ lines) are mixed. From the spectra, decrease of N and increase of O with the increase of T_S were roughly suggested, although precise evaluation is hard due to mixing of the peaks with the peaks of V. Then I fitted the spectra with four Gaussian corresponding to $N_{K\alpha}$, V_{Ll} , $V_{L\alpha}$ and $O_{K\alpha}$ lines. The peak positions and peak widths of V_{Ll} and $V_{L\alpha}$ were fixed based on the spectrum of V metal. Those of $N_{K\alpha}$ and $O_{K\alpha}$ were fixed based on the spectra of the films with $T_S = 400$ °C and 450 °C, because they showed strong nitrogen peaks. The ratio of peak intensities between V_{Ll} and $V_{L\alpha}$ lines were also fixed. Fitted peaks are shown in Fig. 3.2b. The monotonic decrease of N peak and increase of O peak against the increase of T_S were apparently observed. Nitrogen peak even got almost zero as T_S increased to 600 °C. This result can be understood by re-evaporation of nitrogen during deposition. Since oxynitride is thermodynamically less stable than oxide, thin film will release nitrogen during fabrication, the rate of which increases with the increase of temperature. Therefore, the film grown at higher T_S is considered to contain less nitrogen due to its high release rate.

Based on the crystallinity and nitrogen content in the thin films, T_S was set at

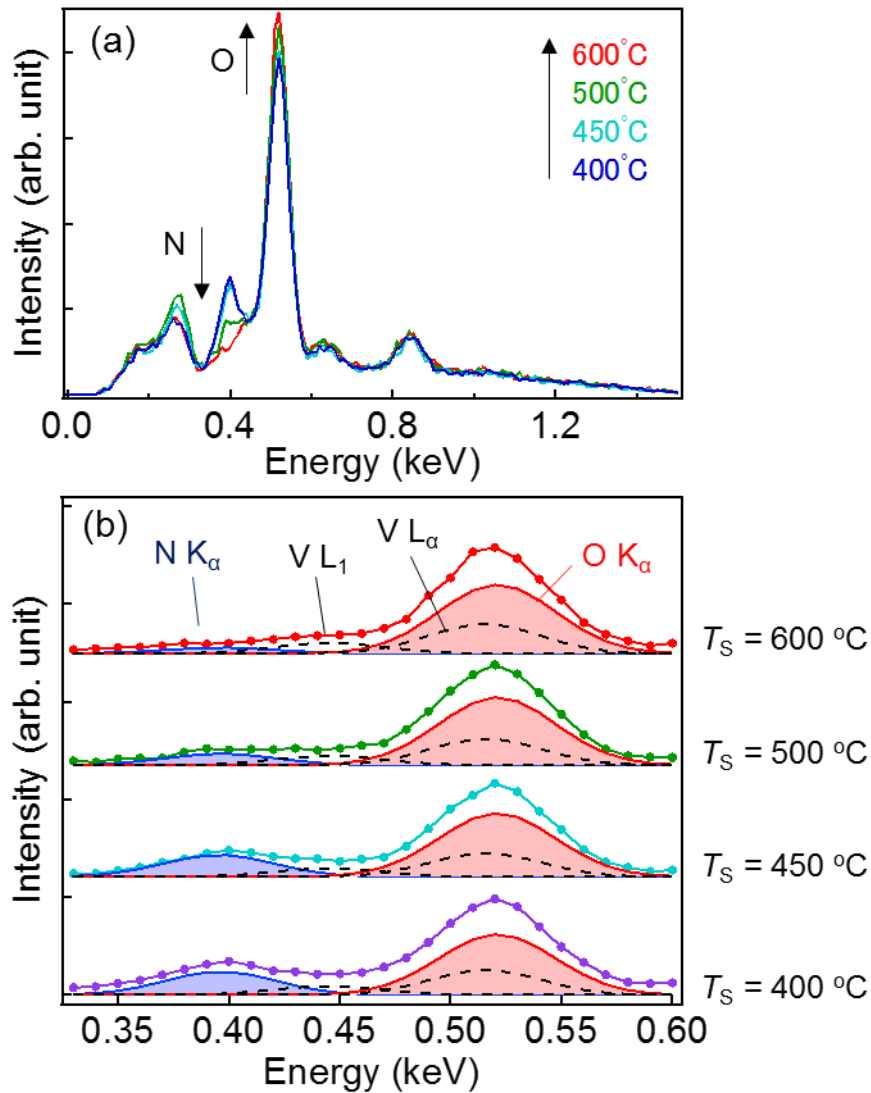


Figure 3.2 (a) EDX spectra of the LVON thin films fabricated at different T_S and (b) part of the spectra fitted with four Gaussians.

500 °C in the following part. The nitrogen content in the thin films was controlled with the input power of RF source and the deposition rate as parameters. Because plasma density increases with the increase of input power of RF source, the power directly contributes to the nitrogen content in the thin film. On the other hand, deposition rate is regarded as supply rate of other elements (La, V and O) and contributes to the supply of nitrogen radical per unit lattice. Based on these contribution, I used input power of RF source normalized by deposition rate as an indicator of nitrogen amount, which is regarded as relative supply rate of nitrogen radical.

Nitrogen content was estimated from NRA measurement with a stoichiometric TiN film as reference. The fabrication conditions and the nitrogen contents of thin films are summarized in table 3.1 and Fig. 3.3. The nitrogen content monotonically increased with an increase of normalized input power of the RF source, indicating that nitrogen content was systematically controlled with the fabrication conditions. The result was not linear, possibly due to re-evaporation of N, which is not proportional to normalized input power of RF source.

Figure 3.4a shows EDX spectra of LVON thin films. I note that the spectrum of LVON thin film with $x = 0.61$ was not included in the figure because it was too thin to be measured. Peak fitting was conducted for the spectra in the same manner as the spectra in Fig. 3.2. The peak intensity of $N_{K\alpha}$ and $O_{K\alpha}$ lines increased and decreased, respectively, with an increase of nitrogen content. The peak intensity of $N_{K\alpha}$ had almost linear relationship with the nitrogen content estimated by NRA as shown in Fig. 3.4b, which supported the estimation. In EDX spectra, even thin film with $x = 0$ showed a finite N peak, but it is probably due to imperfect fitting. The O/V and La/V ratio of peak intensity were plotted in Fig. 3.4c. O/V monotonically decreased with the increase of N content. As is evident from the O/V values, total anion content ($x + y$ in $LaVO_yN_x$) is almost 3 in all samples, which suggests that nitrogen is not intercalated but substituted for oxygen. On the other hand, the La/V value was almost constant in all thin films, which means that La/V ratio is not changed within the fabrication conditions.

Figure 3.5a compares the $2\theta - \theta$ XRD patterns of the LVON thin films with different nitrogen content. Only peaks which correspond to $00n$ diffraction of perovskite-type structure appeared in all thin films. The patterns indicate fabrication of phase pure single crystalline LVON thin films without impurity. The full width at half maximum (FWHM) value of the rocking curves of the 002 diffractions were 0.05-0.07°, indicating high crystallinity of the thin films. The peak position of the thin films shifted to smaller

Table 3.1 The fabrication conditions and the nitrogen contents of the LVON thin films.

sample number	input power of RF source (W)	deposition rate (nm/h)	Normalized input power (W (nm/h) ⁻¹)	x in LaVO _{3-x} N _x
1	0	30	0	0
2	100	24	4.2	0.18
3	200	23	8.7	0.29
4	300	17	18	0.44
5	400	14	28	0.61
6	400	9.4	42	0.71

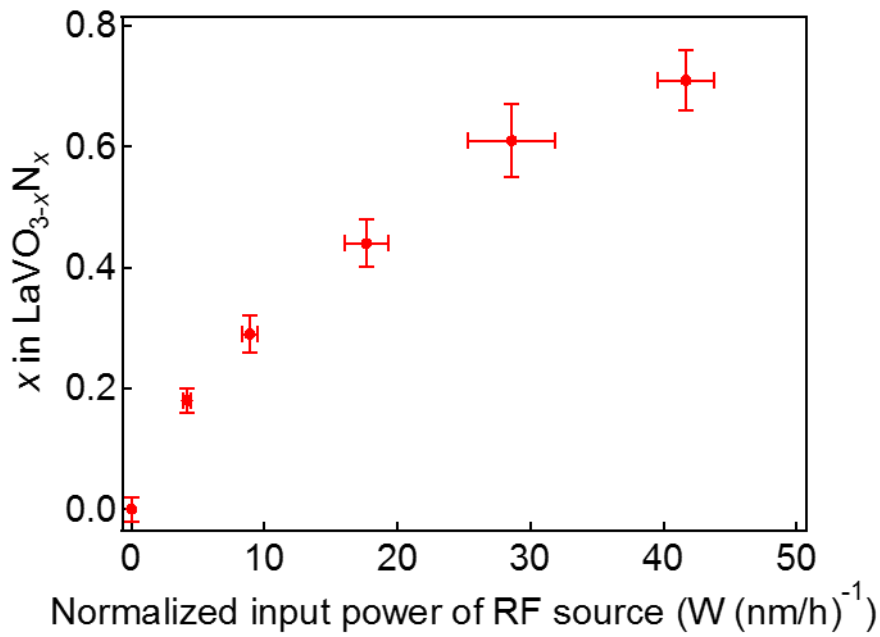


Figure 3.3 Nitrogen amount in the LVON thin films plotted as function of the input power of RF source normalized by the deposition rate of the film. Error bars reflect the uncertainty of film thickness and the systematic error of NRA measurement.

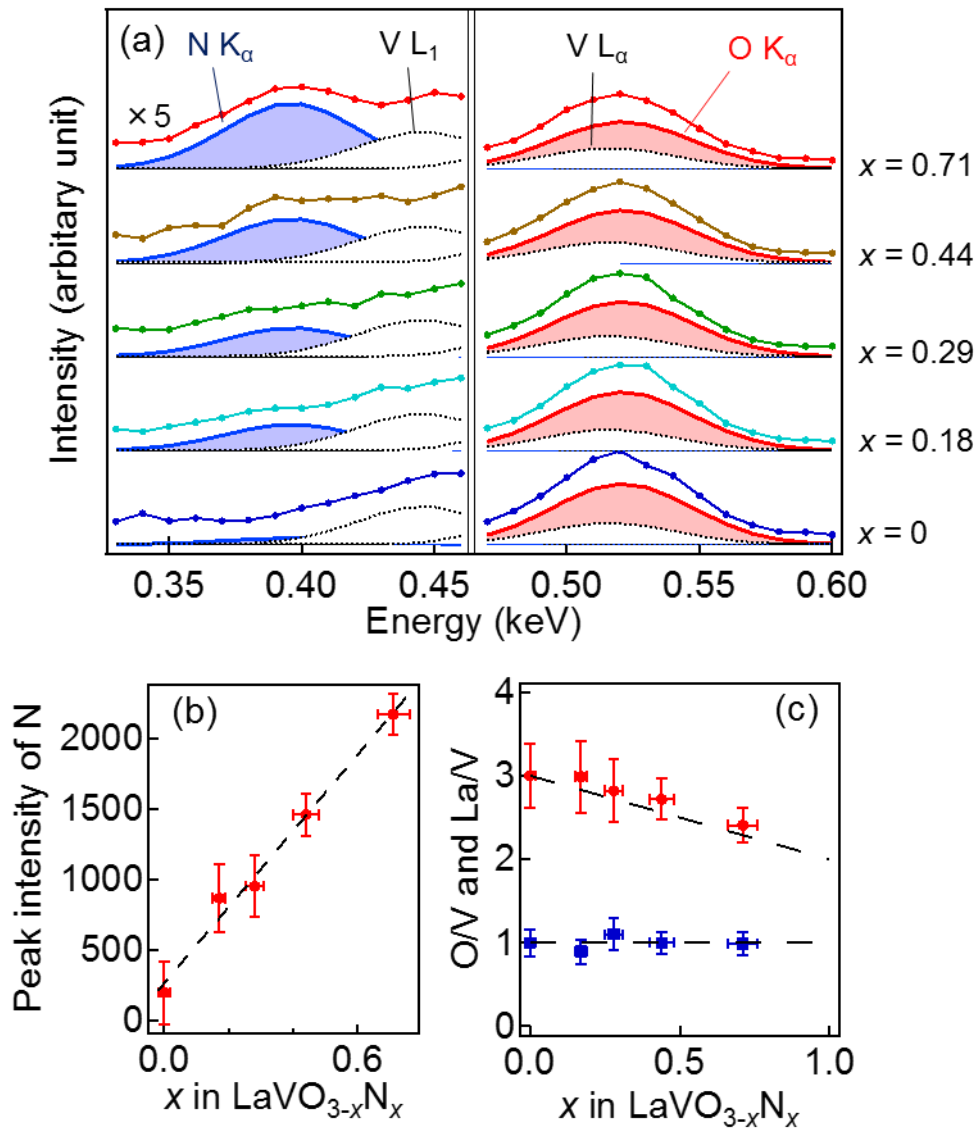


Figure 3.4 (a) EDX spectra of the LVON thin films. The intensity of signals in left half were enlarged five times. (b) The peak intensity of N plotted as function of nitrogen amount estimated from NRA measurement. (c) The $O_{K\alpha}/V_{L\alpha}$ ratio (circles) and $La_{M\alpha}/V_{L\alpha}$ ratio (squares) plotted as function of nitrogen amount. The ratios were normalized by the thin film with $x=0$ so that $O/V=3$ and $La/V=1$. Dashed lines show stoichiometric composition represented as $LaVO_{3-x}N_x$.

angle side with the increase of nitrogen content x . It indicates that the lattice shrinks with the increase of x , consistent with the report on bulk LVON [37]. In order to determine lattice constants of the LVON thin films, X-ray RSM was performed. Figure 3.5b shows the reciprocal space map of the LVON film ($x = 0.71$) around LVON 301 peak. The crystal lattice of the LVON thin film showed tetragonal distortion caused by the compressive strain from the substrate. In-plane lattice constant was perfectly locked to the substrate, indicating coherent growth. Coherent growth was observed in all LVON films.

The lattice volumes of LVON thin films calculated from their RSM measurement were plotted as a function of x in Fig. 3.6. The volume of the undoped one agrees well with a previous report on a stoichiometric LaVO_3 coherently grown on an LSAT substrate [68], indicating stoichiometric La/V in the LaVO_3 film. Since La/V ratio was almost the same in all films as mentioned in Fig. 3.4c, stoichiometric cation ratio was confirmed in all LVON films. Then the lattice volumes of the LVON thin films were compared with those of bulk LVONs. Since lattice volume of thin film under epitaxial strain should be different from that of bulk material free from distortion, I estimated the lattice volume of LVON strained by biaxial force, based on the previously reported bulk data. Bulk LVON was assumed as cubic. In-plane lattice constant of the strained LVON was set at the lattice constant of an LSAT substrate (3.868 \AA), because all my thin films were grown coherently. In this estimation, Poisson's ratio, which determines out-of-plane lattice constant of the strained LVON, was assumed to be 0.3, which is a typical value for oxide [69]. The observed lattice volume of the LVON thin films were consistent with the estimated one as shown in Fig. 3.6, supporting that nitrogen is not intercalated in the lattice but substituted for oxygen site.

Atomic-scale surface morphology of the LVON thin films was observed by AFM. Figure 3.7 shows the surface image of LVON ($x = 0.71$) thin film on LSAT (100) and STO (100) substrates. No grain structure was observed on both thin films, and they were

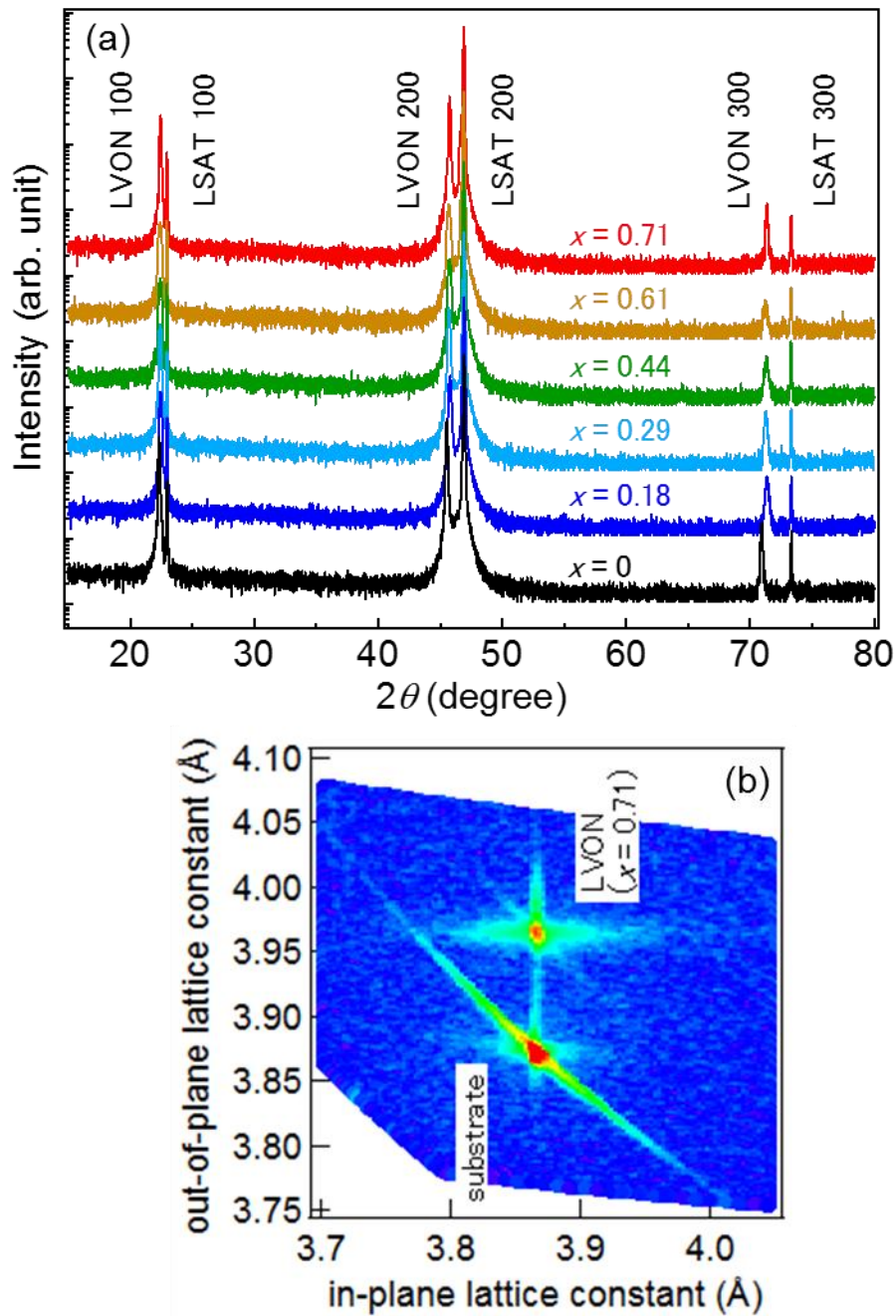


Figure 3.5 (a) XRD patterns of the LVON thin films grown on LSAT (100) substrates. (b) RSM around the 301 diffractions of LVON ($x = 0.71$) thin film and the LSAT (100) substrate.

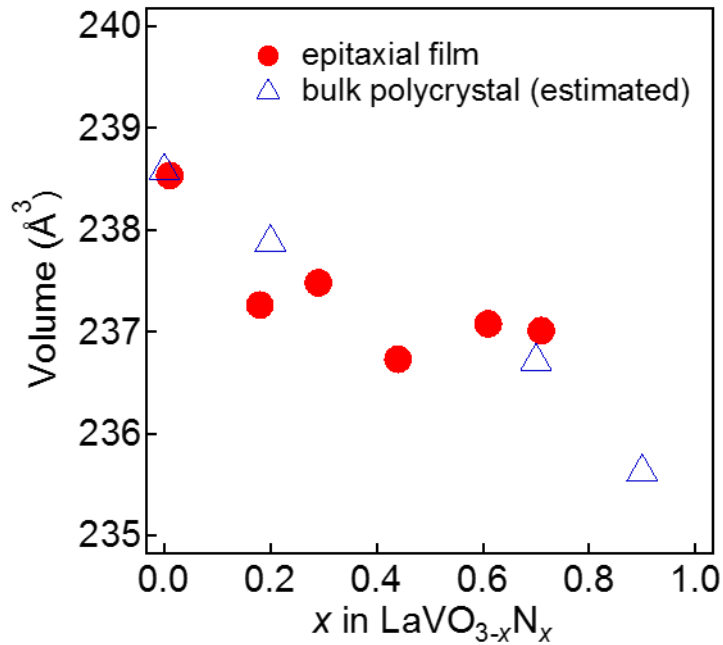


Figure 3.6 Lattice volume of the LVON thin films grown on LSAT substrates (circles) and LVON polycrystal (triangles) plotted as function of nitrogen amount. The values of bulk polycrystals were estimated from the lattice volumes of bulk LVONs [37] with Poisson's ratio of 0.30.

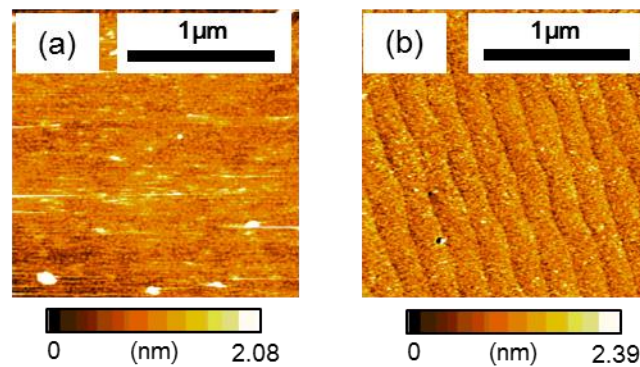


Figure 3.7 AFM images of LVON ($x = 0.71$) thin films grown on (a) LSAT (100) and (b) STO (100) substrates.

atomically flat. Moreover, in the case of the thin films fabricated on an STO (100) substrate, clear step-and-terrace structure appeared, which reflects the surface morphology of the substrate with the same structure. These results indicate Frank-van der Merwe growth mode for the thin films and little grain boundary in them.

Flatness of the thin films was also confirmed from clear thickness fringes in their XRD patterns which was observed with 0D-detector (Fig. 3.8). The period of the fringes was consistent with the thickness of the thin films measured with the stylus profiler.

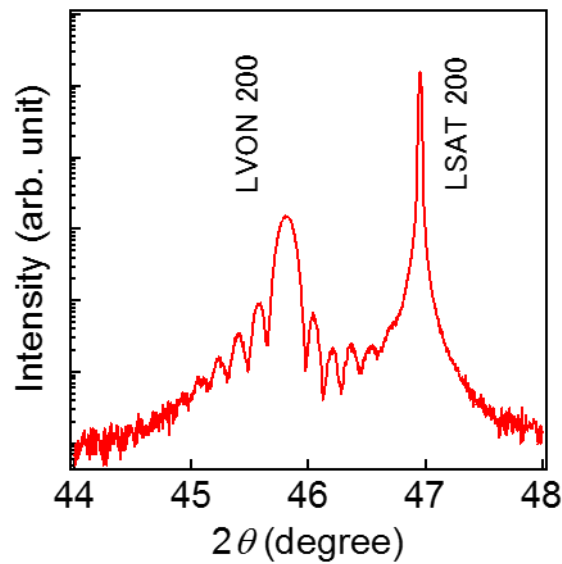


Figure 3.8 XRD pattern of the LVON ($x = 0.71$) film grown on an LSAT (100) substrate observed with 0D detector.

3.3.2 Transport properties of $\text{LaVO}_{3-x}\text{N}_x$

The crystal structure and the surface morphology indicate little grain boundary in the LVON thin films. Then I measured resistivity for investigation of intrinsic transport properties.

First, I investigated carrier type in LVON from the sign of its Seebeck coefficient, and the carrier was found to be hole. This carrier type is consistent with nitrogen doping, in which trivalent nitride ion is substituted for divalent oxide ion.

Figure 3.9a shows the resistivity (ρ) of my LVON epitaxial thin films and previously reported LVON bulk polycrystals [37,59] at 300K. The ρ values of the LVON thin films were 2 or 3 orders of magnitude smaller than those of the LVON bulk polycrystals. This resistivity drop suggests suppression of grain boundary scattering, although the other origins such as lattice deformation cannot be excluded.

Figure 3.9b shows temperature dependence of ρ . All LVON thin films showed negative slope, indicating that LVON was still semiconducting even if hole was heavily doped ($x = 0.71$). This result is quite different from the case of cation-site substituted material $\text{La}_{1-z}\text{Sr}_z\text{VO}_3$ (LSVO) [55,56] and $\text{La}_{1-z}\text{Ca}_z\text{VO}_3$ (LCVO) [57,58], because LSVO and LCVO show IMT with much smaller doping level ($z = 0.18$ and 0.26 , respectively). Furthermore, the ρ value of LVON was higher than that of LSVO with the same doping level. These results indicate that carriers in LVON were localized as an intrinsic feature of LVON, not originating from grain boundary scattering.

Next, I discuss the origin of the carrier localization specific to LVON. To determine the conduction mechanism of LVON, I focused on the temperature dependence of ρ . It is different with the conduction mechanism, and, in most cases, it is represented by the following formula;

$$\rho = \rho_0 \exp(-aT^\nu) \quad (3.1)$$

where ν is a conduction-model-dependent parameter. Therefore, conduction

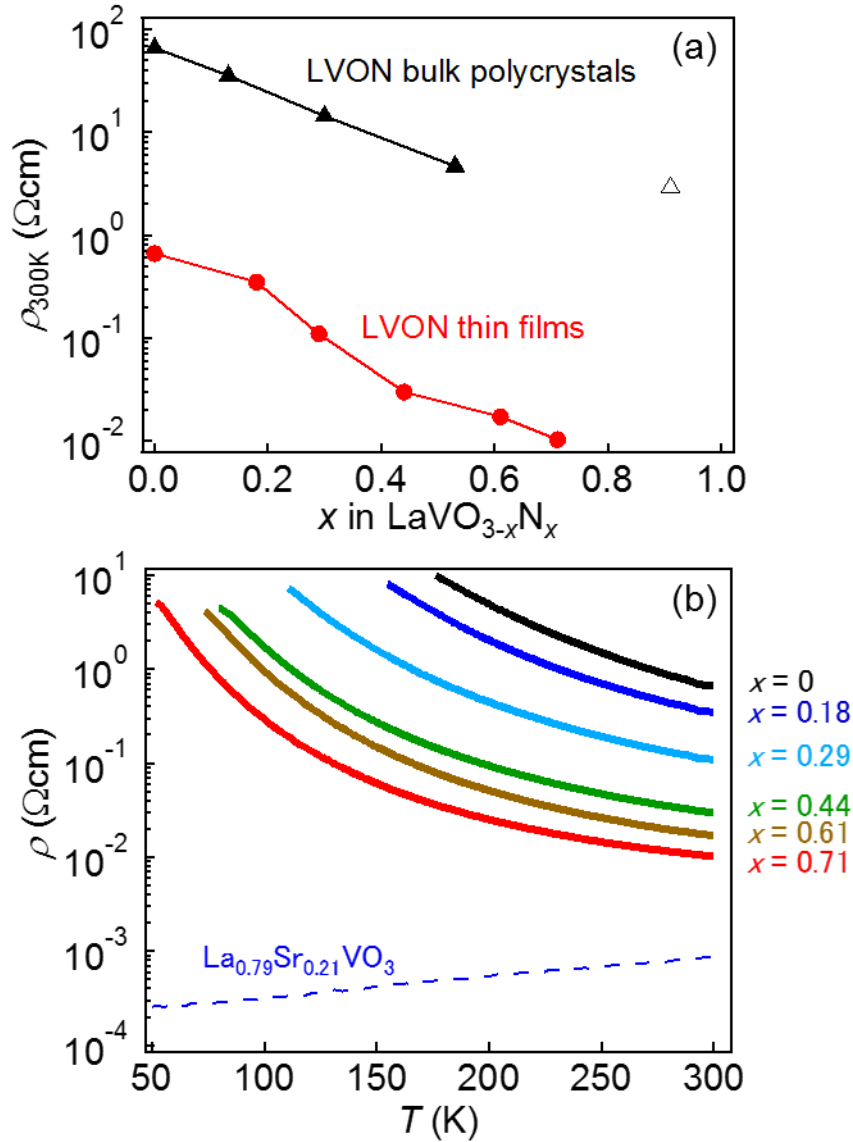


Figure 3.9 (a) Resistivity of the LVON thin films (filled circles) and LVON bulk polycrystals (solid [37] and blank [59] triangles) measured at 300K plotted as functions of nitrogen amount. (b) Resistivity of the LVON thin films (solid) and $\text{La}_{0.79}\text{Sr}_{0.21}\text{VO}_3$ single crystal (dashed) [55] plotted as functions of temperature.

mechanism can be estimated from the value of ν .

The value of ν is determined directly by plotting $\log[-\partial\ln(\rho)/\partial\ln(T)]$ against $\log(T)$, because the linear slope of the plot gives ν [70]. Figure 3.10 shows the plot for LVON with $x = 0.71$. The plot indicates $\nu = -1$ and $\nu = -1/2$ in a range of $T > 170$ K and $T < 170$ K, respectively. $\nu = -1$ corresponds to thermally activated band conduction

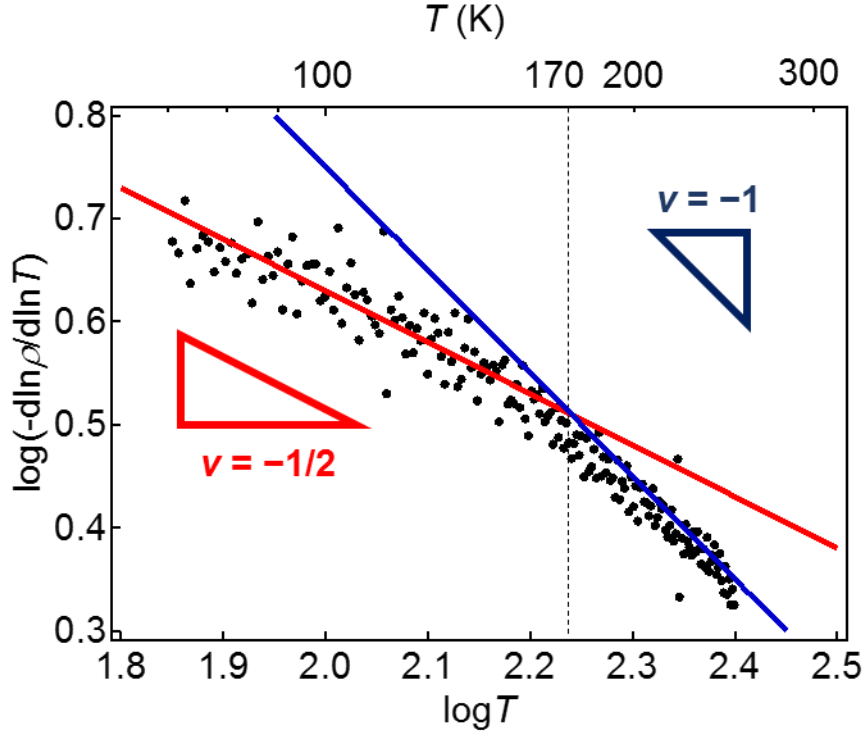


Figure 3.10 $\log[-\partial \ln(\rho)/\partial \ln(T)] - \log(T)$ plot for the LVON thin film ($x = 0.71$) grown on an LSAT (100) substrate.

(known as Arrhenius law) or nearest neighbor hopping conduction. They are appropriate as high temperature phase because they need thermal energy, although it is difficult to distinguish them. On the other hand, $\nu = -1/2$ was different from 3D-VRH ($\nu = -1/4$), which is widely observed in doped Mott insulators with semiconducting behavior [58]. The conduction mechanisms which show $\nu = -1/2$ are 1-dimensional variable range hopping (1D-VRH) and Efros-Shklovskii variable range hopping (ES-VRH). However, neither is suited to this case for the following reasons. First, LVON did not have 1-dimensional structure necessary for 1D-VRH. Second, ES-VRH should be observed only at much lower temperature (< 10 K) [10].

Thus, I attribute the carrier localization observed for LVON to another kind of conduction, to which I refer as “pseudo Efros-Shklovskii type (pseudo-ES-type)” conduction. This conduction shows $\nu = -1/2$ over a wide range of temperatures and has recently been reported in some strongly correlated electron systems with large disorder

[70-72]. Although the cause of this conduction is not well understood, it is suggested that electron correlation and disorder are responsible for the conduction like ES-VRH. LVON satisfies these conditions well because of the following reasons. First, as its parent material LaVO_3 belongs to Mott insulator, electron correlation will be strong in LVON. Second, nitrogen is randomly substituted for oxygen-site, which is a part of VX_6 conduction path, in LVON. Substitution of nitrogen possibly induces strong random potential to the conduction path. This is quite different from the case of La-site doping, because La-site is not included in the conduction path. Since first condition is common in doped LaVO_3 , disorder is expected as a key factor for carrier localization in LVON. Indeed, a similar situation was encountered in a V-site substituted LVO ($\text{LaV}_{1-x}\text{Ti}_x\text{O}_3$), which is semiconductor over wide compositional range ($0 \leq x \leq 0.75$). [73]. Therefore, I concluded that carrier localization in LVON originated from strongly disordered potential by random substitution of N.

3.4 Summary

Pure and stoichiometric perovskite-type $\text{LaVO}_{3-x}\text{N}_x$ epitaxial thin films with nitrogen content controlled from 0 to 0.71 were fabricated with NPA-PLD method for measurement of intrinsic transport properties. The films showed high crystallinity and flat surface structure, which are favored for measurement of transport properties. While the contribution of grain boundary should be reduced, the LVON films were still semiconductor, which indicates intrinsic carrier localization in LVON. This is supposed to be attributed to disordered potential due to random substitution of N. This suggests one possibility that conductivity of perovskite-type oxynitride is enhanced by reducing the disorder in potential.

Chapter 4

Formation of oxide/oxynitride superlattice for remote doping

本章については、5年以内に雑誌等で刊行予定のため、非公開。

Chapter 5

Topotactic nitridation of layered perovskite oxide for anion-ordered structure

本章については、5年以内に雑誌等で刊行予定のため、非公開。

Chapter 6

General conclusion

In this thesis, I investigated the transport properties of perovskite-type oxynitride using epitaxial thin film growth technique.

Intrinsic carrier transport properties in perovskite-type oxynitride $\text{LaVO}_{3-x}\text{N}_x$

Perovskite-type $\text{LaO}_{3-x}\text{N}_x$ single crystalline thin films with a wide variety of nitrogen contents ($0 \leq x \leq 0.71$) were synthesized with NPA-PLD method. Intrinsic carrier localization was confirmed from resistivity measurements. From the temperature dependence of resistivity, it was indicated that the carrier localization was due to the disordered potential associated with randomly substituted nitrogen. This suggests that the conductivity of perovskite-type oxynitride can be enhanced by suppressing the disorder in potential.

Formation of oxide/oxynitride superlattice for remote doping

Superlattice structures of LaVO_3 and $\text{LaVO}_{3-x}\text{N}_x$ were fabricated by applying NPA-PLD method. Observation of satellite peaks in XRD patterns and periodic anion distribution by SIMS proved that the superlattice structures were successfully constructed, although N contamination was seen. The superlattice showed higher conductance than the sum of individual layers, suggesting contribution of remote carrier doping to the overall conduction. Similar result was obtained for the conductivity of $\text{LaVO}_3/\text{LaVO}_{3-x}\text{N}_x$ single heterostructure, where nitrogen contamination was neglected, validating the additional conduction at the interface.

Topotactic nitridation of layered perovskite oxide for anion-ordered structure

$\text{La}_2\text{Ti}_2\text{O}_7$ and Sm_2TiO_7 thin films with layered perovskite structure were subjected to further nitridation by ammonolysis method. By the ammonolysis method, these $\text{La}_2\text{Ti}_2\text{O}_7$ and Sm_2TiO_7 were transformed to perovskite-type LaTiO_2N and SmTiO_2N , respectively, in a topotactic manner. Therefore, nitridation of layered perovskite oxide single crystalline thin film was a promising new route to fabricate perovskite-type oxynitride in single crystalline thin film form, although reaction temperature needs to be lowered for anion ordering.

Through the researches on single crystalline perovskite-type $\text{LaVO}_{3-x}\text{N}_x$, I unveiled carrier location as its intrinsic nature governing the transport properties. From the temperature dependence of conductivity, it was concluded that the carrier localization was caused by disordered potential originating from randomly substituted N. As an approach for increasing the conductivity of oxynitrides, I proposed remote carrier doping by forming oxide/oxynitride stacked structure such as superlattice and heterostructure. The non-negligible contribution of conduction at the interface to the overall conductance was suggested from conductance measurement. Another way for increasing the conductivity of oxynitrides is to suppress the random potential in oxynitrides by ordering anions. I tried to synthesize crystalline perovskite-type oxynitrides by ammonolysis of layered perovskite oxide as a precursor, where nitrogen ordering along the excess oxygen layer was expected. Although the transformation of layered perovskite oxide to perovskite oxynitride successfully proceeded, nitrogen was suggested to be randomly distributed possibly due to high reaction temperature. I also attempted to achieve nitrogen ordering in oxynitride with the use of epitaxial strain, and I succeeded in fabricating perovskite-type oxynitride with possible partial anion order (Appendix Chapter A). On the basis of

this study, I concluded that perovskite-type oxynitride is an attractive compound which shows specific transport properties, different from cation-site substituted compounds, and that they can be modified through controlling anion distribution.

Appendix Chapter A

Fabrication of perovskite-type oxynitride with large lattice distortion

本章については、5年以内に雑誌等で刊行予定のため、非公開。

Bibliography

- [1] K. Momma and F. Izumi, *J. Appl. Crystallogr.* **44**, 1272 (2011).
- [2] A. S. Bhalla, R. Guo and R. Roy, *Mat Res Innovat.* **4**, 3 (2000).
- [3] A. M. Glazer, *Acta Cryst. B* **28**, 3384 (1972).
- [4] F. Lichtenberg, A. Herrnberger and K. Wiedenmann, *Progress in Solid State Chemistry* **36**, 253 (2008).
- [5] T. N. Bondarenko, V. N. Uvarov, S. V. Borisenko, Y. A. Teterin, V. P. Dzeganovski, A. M. Sych and Y. A. Titiv, *J. Korean Phys. Soc.* **32**, S65 (1998).
- [6] A. Bayart, A. Katelnikovas, J-F. Blach, J. Rousseau and S. Saitzek, *J. Alloys Compd.* **683**, 634 (2016).
- [7] B. Bhushan, A. Basumallick, S. K. Bandopadhyay, N. Y. Vasanthacharya and D. Das, *J. Phys. D: Appl. Phys.* **42**, 065004 (2009).
- [8] A. Gautam and V. S. Rangra, *Cryst. Res. Technol.* **45**, 953 (2010).
- [9] M. Yang J. Oró-Solé, A. Kusmartseva, A. Fuertes and J. P. Attfield, *J. Am. Chem. Soc.* **9** 4823 (2010).
- [10] B. Sandow, K. Gloos, R. Rentzsch, A. N. Ionov and W. Schirmacher, *Phys. Rev. Lett.* **86**, 1845 (2001).
- [11] M. Brahlek, L. Zhang, J. Lapano, H. Zhang, R. Engel-Herbert, N. Shukla, S. Datta, H. Paik and D. G. Schlom, *MRS communications* **7**, 27 (2017).
- [12] A. Wilson, *Proc. Roy. Soc. A* **133**, 458 (1931).
- [13] N. F. Mott, *Proc. Phys. Soc. A* **62** 416 (1949).
- [14] N. F. Mott, *Rev. Mod. Phys.* **40**, 677 (1968).
- [15] M. Imada, A. Fujimori and Y. Tokura, *Rev. Mod. Phys.* **70**, 1039 (1998).
- [16] M. Medarde, J. Mesot, S. Rosenkranz, P. Lacorre, W. Marshall, S. Klotz, J. S.

- Loveday, G. Hamel, S. Hull and P. Radaelli, *Physica B* **15**, 234 (1997).
- [17] J. L. García-Muñoz, J. Rodríguez-Carvajal, P. Lacorre and J. B. Torrance, *Phys. Rev. B* **46**, 4414 (1992).
- [18] P. Lacorre, J. B. Torrance, J. Pannetier, A. I. Nazzal, P. W. Wang and T. C. Huang, *J. Solid State Chem.* **91**, 225 (1991).
- [19] C. Eylem, H. L. Ju, B. W. Eichhorn and R. L. Greene, *J. Solid State Chem.* **114**, 164 (1995).
- [20] D. M. Newns, J. A. Misewich, C. C. Tsuei, A Gupta, B. A. Scott and A. Schrott, *Appl. Phys. Lett.* **73**, 780 (1998).
- [21] J. Fujioka, S. Miyasaka and Y. Tokura, *Phys. Rev. B* **72**, 024460 (2005).
- [22] A. Ohtomo and H. Y. Hwang, *Nature* **427**, 423 (2004).
- [23] J. Biscaras, N. Bergeal, A. Kushwaha, T. Wolf, A. Rastogi, R. C. Budhani and J. Lesueur, *Nat. Commun.* **1**, 89 (2010).
- [24] J. S. Kim, S. S. A. Seo, M. F. Chisholm, R. K. Kremer, H. -U. Habermeier, B. Keimer and H. N. Lee, *Phys. Rev. B* **82**, 201407 (2010).
- [25] W. C. Sheets, Ph. Boullay, U. Lüders, B. Mercey and W. Prellier, *Thin Solid Films* **517**, 5130 (2009).
- [26] T. Mimura, S. Hiyamizu, T. Fujii and K. Nanbu, *Jpn. J. Appl. Phys.* **19**, L225 (1980).
- [27] S. Hiyamizu, T. Mimura, T. Fujii and K. Nanbu, *Appl. Phys. Lett.* **37**, 805 (1980).
- [28] M. Okuyama, T. Ueda and Y. Hamakawa, *Jpn. J. Appl. Phys.* **24**, 619 (1985).
- [29] S. Havelia, S. Wang, K. R. Balasubramaniam and P. A. Salvador, *J. Solid State Chem.* **182**, 1603 (2009).
- [30] Z. Shao, S. Saitzek, A. Ferri, M. Rguiti, L. Dupont, P. Roussel and R. Desfeux, *J. Mater. Chem.* **22**, 9806 (2012).
- [31] T. Ukita, Y. Hirose, S. Ohno, K. Hatabayashi, T. Fukumura and T. Hasegawa, *J. Appl. Phys.* **111**, 07D909 (2012).

- [32] M. Al-Mamouri, P. P. Edwards, C. Greaves and M. Slaski, *Nature* **369**, 382 (1994).
- [33] S. Yoon, A. E. Maegli, A. Eyssler, M. Trottmann, T. Hisatomi, C. M. Leroy, M. Grätzel and A. Weidenkaff, *Energy Procedia* **22**, 41 (2012).
- [34] K. Maeda and K. Domen, *Bull. Chem. Soc. Jpn.* **89**, 627 (2016).
- [35] J. Xu, C. Pan, T. Takata and K. Domen, *Chem. Commun.* **51**, 7191 (2015).
- [36] D. Oka, Y. Hirose, H. Kamisaka, T. Fukumura, K. Sasa, S. Ishii, H. Matsuzaki, Y. Sato, Y. Ikuhara and T. Hasegawa, *Sci. Rep.* **4**, 4987 (2014).
- [37] P. Antoine, R. Assabaa, P. L'haridon, R. Marchand and Y. Laurent, *Mater. Sci. Eng. B* **5**, 43 (1989).
- [38] D. Logvinovich, J. Hejtmanek, K. Knizek, M. Marysko, N. Homazava, P. Tomes, R. Aguiar, S. G. Ebbinghaus, A. Reller and A. Weidenkaff, *J. Appl. Phys.* **105**, 023522 (2009).
- [39] L. Balcells, J. Navarro, M. Bibes, A. Roig, B. Martinez and J. Fontcuberta, *Appl. Phys. Lett.* **78**, 781 (2001)
- [40] H. M. Rietveld, *J. Appl. Cryst.* **2**, 65 (1969).
- [41] M. Yang, J. Oro-Sole, J. A. Rodgers, A. B. Jorge, A. Fuertes and J. P. Attfield, *Nat. Chem.* **3**, 47 (2011).
- [42] J. Oro-Sole, L. Clark, W. Bonin, J. P. Attfield and A. Fuertes, *Chem. Commun.* **49**, 2430 (2013).
- [43] D. Oka, Y. Hirose, F. Matsui, H. Kamisaka, T. Oguchi, N. Maejima, H. Nishikawa, T. Muro, K. Hayashi and T. Hasegawa, *ACS Nano* **11**, 3860 (2017).
- [44] A. Fuertes, *J. Mater. Chem.* **22**, 3293 (2012).
- [45] F. Tessier and R. Marchand, *J. Solid State Chem.* **171**, 143 (2003).
- [46] I. Takano, *J. Surf. Finish. Soc. Jpn.* **52**, 805 (2001).
- [47] K. Yamada, H. Nakamura, S. Matsushima, H. Yamane, T. Haishi, K. Ohira and K. Kumada, *C. R. Chemie* **9**, 788 (2006).

- [48] K. Kato, H. Kondo, M. Sakashita and S. Zaima, *Thin Solid Films* **518**, S226 (2010).
- [49] K. Watanabe and T. Tatsumi, *Appl. Phys. Lett.* **76**, 2940 (2000).
- [50] M. Pichler, W. Si, F. Haydous, H. Téllez, J. Druce, E. Fabbri, M. E. Kazzi, M. Döbeli, S. Ninova, U. Aschauer, A. Wokaun, D. Pergolesi and T. Lippert, *Adv. Funct. Mater.* **27**, 1605690 (2017)
- [51] I. Marozau, A. Shkabko, M. Döbeli, T. Lippert, D. Logvinovich, M. Mallepell, C. W. Schneider, A. Weidenkaff and A. Wokaun, *Materials* **2**, 1388 (2009).
- [52] I. Marozau, A. Shkabko, M. Döbeli, T. Lippert, M. Mallepell, C. W. Schneider, A. Weidenkaff and A. Wokaun, *Acta Materialia* **59**, 7145 (2011).
- [53] D. Oka, Y. Hirose, T. Fukumura and T. Hasegawa, *Cryst. Growth Des.* **14**, 87 (2014).
- [54] T. Arima and Y. Tokura, *J. Phys. Soc. Jpn.* **64**, 2488 (1995).
- [55] S. Miyasaka, T. Okuda and Y. Tokura, *Phys. Rev. Lett.* **85**, 5388 (2000).
- [56] F. Inaba, T. Arima, T. Ishikawa, T. Katsufuji, and Y. Tokura, *Phys. Rev. B* **52**, R2221 (1995).
- [57] H. Nguyen and J. Goodenough, *Phys. Rev. B* **52**, 8776 (1995).
- [58] K Maiti, N. Vasanthacharya and D. Sarma, *J. Phys.: Condens. Matter* **9**, 7507 (1997).
- [59] J. Oro-Sole, L. Clark, N. Kumar, W. Bonin, A. Sundaresan, J. Attfield, C. Rao and A. Fuertes, *J. Mater. Chem. C* **2**, 2212 (2014).
- [60] S. G. Ebbinghaus, R. Aguiar, A. Weidenkaff, S. Gsell and A. Reller, *Solid State Sciences* **10**, 709 (2008).
- [61] C. Izawa and T. Watanabe, *Chem. Lett.* **43**, 1441 (2014).
- [62] W. Prellier, A. Fouchet, B. Mercey, Ch. Simon and B. Raveau, *Appl. Phys. Lett.* **82**, 3490 (2003).
- [63] D. Craciun, N. Stefan, G. Socol, G. Dorcioman, E. McCumiskey, M. Hanna, C. R. Taylor, G. Bourne, E. Lambers, K. Siebein and V. Craciun, *Appl. Surf. Sci.* **260**, 2 (2012).
- [64] L. Guan, D. Zhang, X. Li and Z. Li, *Nucl. Instrum. Meth. B* **266**, 57 (2008).

- [65] A. Suzuki, Y. Hirose, D. Oka, S. Nakao, T. Fukumura, S. Ishii, K. Sasa, H. Matsuzaki and T. Hasegawa, *Chem. Mater.* **26**, 976 (2014).
- [66] J. Takahashi, Y. Hirose, D. Oka, S. Nakao, C. Yang, T. Fukumura, I. Harayama, D. Sekiba and T. Hasegawa, *Appl. Phys. Lett.* **107**, 231906 (2015).
- [67] S. Hasegawa, "Reflection High-Energy Electron Diffraction", *Characterization of Materials*, 1925 (2012).
- [68] M. Brahlek, L. Zhang, H. Zhang, J. Lapano, L. Dedon, L. Martin and R. Engel-Herber, *Appl. Phys. Lett.* **109**, 101903 (2016).
- [69] G. N. Greaves, A. L. Greer, R. S. Lakes and T. Rouxel, *Nat. Mater.* **10**, 823 (2011).
- [70] A. Rogatchev and U. Mizutani, *Phys. Rev. B* **61**, 15550 (2000).
- [71] H. Shinaoka and M. Imada, *J. Phys. Soc. Jpn.* **78**, 094708 (2009).
- [72] S. Nakatsuji, V. Dobrosavljevic, D. Tanaskovic, M. Minakata, H. Fukazawa and Y. Maeno, *Phys. Rev. Lett.* **93**, 146401 (2004).
- [73] C. Eylem, Y.-C. Hung, H. L. Ju, J. Y. Kim, D. C. Green, T. Vogt, J. A. Hriljac, B. W. Eichhorn, R. L. Greene and L. Salamanca-Riba, *Chem. Mater.* **8**, 418 (1996).
- [74] W. Zhao, Y. Qi, T. Sajoto, S. Barlow, S. R. Marder and A. Kahn, *Appl. Phys. Lett.* **97**, 123305 (2010).
- [75] J. M. Ramírez, J. Wojcik, Y. Berencén, A. Ruiz-Caridad, S. Estradé, F. Peiró, P. Mascher and B. Garrido, *Nanotechnology* **26**, 085203 (2015).
- [76] A. M. Hartel, D. Hiller, S. Gutsch, P. Löper, S. Estradé, F. Peiró, B. Garrido and M. Zacharias, *Thin Solid Films* **520**, 121 (2011).
- [77] F. Izumi and K. Momma, *Solid State Phenom.* **130**, 15 (2007).
- [78] S. Havelia, S. Wang, K. R. Balasubramaniam and P. A. Salvador, *Cryst. Growth Des.* **9**, 4546 (2009).
- [79] R. D. Shannon, *Acta Cryst. A* **32**, 751 (1976).